Applied Nanoscience (2023) 13:3975–3992
https://doi.org/10.1007/s13204-022-02663-8

ORIGINAL ARTICLE

Mixed-phase of mesoporous titania nanoparticles as visible-light driven photodegradation of 2-chlorophenol: influence type of surfactant

N. A. Marfur[1] · N. F. Jaafar[1] · J. Matmin[2]

Received: 4 April 2022 / Accepted: 21 September 2022 / Published online: 7 October 2022

Abstract

Mesoporous titania nanoparticles (MTN) were prepared using different surfactants namely anionic (MTN-A), cationic (MTN-C) and nonionic (MTN-NI) surfactants via microwave-assisted method to degrade 2-chlorophenol (2-CP) under visible light irradiation. The catalysts were characterised by XRD, FTIR, UV-Vis DRS, PL, BET, FESEM, TEM and XPS. The mesoporous structures were successfully formed in all catalysts with high surface area. However, the significant difference between the prepared catalysts was the formation of mixed-phase in MTN-A which used sodium dodecyl sulfate (SDS) as anionic surfactant. MTN-A composed of 20% rutile and 80% anatase phase. MTN-A showed remarkable photoactivity due to the abundance of Ti^{3+} site defects (TSD) and oxygen vacancies (OV) on its TiO_2 mixed-phase structures. The synergistic effect between the TSD, OV and TiO_2 mixed-phase have improved the electronic band structure, aided the charge migration and reduced the electron–hole recombination rate, thus increasing its photoactivity. Moreover, MTN-A exhibited the best performance with 85% degradation compared to MTN-C, MTN-NI and pretreated commercial TiO_2, Degussa P25 (P25) with 77%, 18% and 62% degradation, respectively. MTN-A also displayed as a promising photocatalyst because it could degrade other chlorophenol derivatives.

Highlights

- Synthesis of MTN using SDS as surfactant generated mixed phase of TiO_2
- Type of surfactant influence the amount of site defects formation on surface of MTN
- Mixed phase and site defects of MTN reduced the electron–hole recombination of MTN
- 2-CP achieved highest degradation with MTN synthesised using anionic surfactant

Keywords Surfactant · Mesoporous titania nanoparticles · Microwave-assisted method · Mixed-phase · Site defects

Introduction

Titania or titanium dioxide is a less toxic, low cost, chemically and thermally stable catalyst. It is commonly used as a photocatalyst during wastewater treatment besides functioning as an active ingredient in sunscreen products (Reinosa et al. 2018; Marfur et al. 2020a; Marfur and Jaafar 2021a; Moharana et al. 2021; Ihnatiuk et al. 2022). However, TiO_2 efficiency is hindered by fast electron–hole recombination and only can be excited by UV-light irradiation due to its wide band gap (Chakhtouna et al. 2021; Khanmohammadi et al. 2021). Generally, TiO_2 also exists in different phases either anatase, rutile, brookite or mixed-phase. Based on the previous studies, anatase which has band gap of 3.20 eV exhibited high photocatalytic performance while rutile which has band gap of 3.02 eV manifested low photocatalytic performance (Savaliya et al. 2022; Noman

✉ N. F. Jaafar
nurfarhana@usm.my

[1] School of Chemical Sciences, Universiti Sains Malaysia, 11800 USM Penang, Malaysia

[2] Department of Chemistry, Faculty of Science, Universiti Teknologi Malaysia, 81310 UTM Johor Bahru, Malaysia

et al. 2019; Marfur et al. 2020c). By modifying the TiO_2 framework, Ti^{3+} site defects (TSD), oxygen vacancies (OV), mesopores and mixed-phase structures can be formed, thus TiO_2 drawbacks can be overcome (Bagheri and Julkapli 2016; Jaafar et al. 2019b; Marfur et al. 2020b; Singh et al. 2021; Wei et al. 2022).

Besides, the electronic band structures of TiO_2 can be enhanced by self-doping with the formation of mixed-phase in the same catalyst framework. Mixed-phase catalyst also can be activated under visible light irradiation due to the effective electron transfer (Kumar et al. 2020; Marfur and Jaafar 2021b; Jamila et al. 2022). According to the previous studies, mixed-phase TiO_2 exhibited a greater photocatalytic performance compared to pure anatase TiO_2 because there is possible electron transfer from anatase to rutile phase. This phenomenon has successfully lowered the rate of carrier recombination in anatase, thus promoting effective electron–hole separation besides contributing to high percentage degradation (Zhou et al. 2019; Assayehegn et al. 2020). Nevertheless, the application of mixed-phase TiO_2 is limited because of its less porous structure, low surface area, difficult synthesis method and low visible light photoactivity (Fu et al. 2018).

Ijadpanah-Saravy et al. (2014) synthesised biphasic TiO_2 nanoparticles via hydrolysis method and calcined at 673K. The proportion of the phases depended on the concentration of sulfate ions. Sulfate ions could change the rutile arrangement to the anatase arrangement by affecting the spatial arrangement pattern of the octahedral. The repulsion between the octahedra could be reduced, thus the ratio of anatase/rutile could be varied. Then, the catalyst was used to degrade cyanide under ultraviolet irradiation. TiO_2 nanoparticles with optimum ratio of 20% rutile and 80% anatase showed the best photocatalytic performance due to the efficient electron transfer.

According to Dong et al. (2020a), mixed-phase mesoporous TiO_2 which contained an abundance of site defects was also proven to perform 4.2 times higher than commercial TiO_2 (Degussa P25). This was due to the formation of mesoporous structure in this catalyst which provided sufficient active sites for the adsorption to take place besides the rutile phase was highly contributed to electron transfer.

Other than that, photocatalysts with porous structure can greatly help in the adsorption of the reactant and enhance the photocatalytic performance (Marfur et al. 2019; Diyuk et al. 2022). According to Jaafar et al. (2015a, b), photocatalytic activity of TiO_2 can be enhanced by modifying its porosity and structures to generate numerous TSD and OV. Its electronic band structures also can be enhanced for application under visible irradiation.

Fu et al. (2018) synthesised mixed-phase mesoporous TiO_2 which has a band gap of 3.1 eV via sol–gel method. This catalyst succeeded in degrading several pollutants under visible light irradiation. There were several factors that contributed to this outstanding photoactivity. Firstly, the formation of mixed-phase lowered the band gap and activated the catalyst under visible light irradiation. The creation of defects at the interface also contributed to narrowing the band gap. Secondly, mesoporous structures with high surface area offered better pollutant adsorption, aided photogenerated charge transport to the surface and reduced electron–hole recombination. Lastly, small crystal size resulted in better redox ability due to quantum-size effect.

One of the dominant parameters that affects the catalyst structure is the surfactant types which can be further classified into anionic, cationic and nonionic. Surfactant usually introduces during the synthesis method to aid the TiO_2 dispersion, help in the structure ordering, prevent agglomeration, constrain grain growth, act as pore template, improve crystallinity as well as control the particles shape and size during the hydrolysis step (Pathak et al. 2013; Wu et al. 2018).

Anionic and cationic surfactants can be differentiated by the charges at the hydrophilic parts which are negative and positive, respectively (Das et al. 2020; Pato et al. 2021). During the synthesis of mesoporous material, organic surfactant molecules will form micelles when they reach above the critical micelle concentration since they possess both hydrophilic and hydrophobic parts. The micelles will eventually become less reactive towards other components that exist in the same environment, thus function as structure directing agents (SDA) to form porous structures within the material. Therefore, surfactant substantially helps during the preparation of the intended material especially for enhancing catalyst morphology since surfactant molecules can assemble and form compartments (Li et al. 2012; Rafiee et al. 2018; Arora and Gupta 2022).

In contrast, for nonionic surfactants, there are hydrophilic parts, but they are not ionised in aqueous solution. While preparing for the intended material, they behave as SDA for macropores and mesopores. The coexistence of macropores and mesopores on the catalyst highly promotes in escalating the mass transport ability, minimising the extent of mesopores passages as well as enlarging the attainable surface area (Li et al. 2014b). In this study, mesoporous titania nanoparticles (MTN) were synthesised using different type of surfactants which are anionic, cationic and nonionic surfactants via microwave-assisted method for photocatalytic degradation of 2-chlorophenol (2-CP) under visible light irradiation. These catalysts were characterised by XRD, FTIR, UV-Vis DRS, PL, BET, FESEM, TEM and XPS.

Experimental

Reagents and material

Titanium (IV) butoxide, commercial TiO_2 (Degussa P25), sodium dodecyl sulfate (SDS), N-cetyl-N,N,N-trimethylammonium bromide (CTAB) and pluronic F127 (F127) surfactants were purchased from Sigma-Aldrich. 2-propanol and hydrochloric acid (HCl) were bought from MERCK, Malaysia. Acetone and methanol were supplied by RPE Reagent pure Erba. Sodium hydroxide (NaOH), ammonium hydroxide (NH_4OH), potassium iodide (KI), sodium oxalate ($Na_2C_2O_4$) and potassium peroxodisulfate ($K_2S_2O_8$) were obtained from QREC™. Phenol, 2-chlorophenol (2-CP), 3-chlorophenol (3-CP), 4-chlorophenol (4-CP) and 2,4-dichlorophenol (2,4-DCP) were acquired from Alfa Aesar, Germany with 99% purity. All these chemicals were of analytical grade and were used without any further purification.

Preparation of catalyst

Mesoporous titania nanoparticles (MTN) were prepared via microwave-assisted method. A 4.68 g of CTAB surfactant was dissolved in 720 mL of distilled water, 120 mL of propanol and 29 mL of 28% ammonia solution. The mixture was kept stirring for half an hour at 323K in the water bath. After 30 min, when the temperature of the water bath had already increased up to 353K, 5.7 mL of titanium (IV) butoxide was added into the mixture and kept stirring for another 2 h in the water bath. The white solution was then transferred into a suitable beaker before being placed in the microwave. The power density of the microwave was 0.56 Wg^{-1}. The heating continued until a sol–gel was formed. The obtained product was collected and dried overnight in an oven before calcining at 873K for 3 h. The final product was then labelled as MTN-C. The experiment was repeated using SDS and F127 surfactants and labelled as MTN-A and MTN-NI, respectively. For comparison, Degussa P25 was calcined for 3 h at 873K and denoted as P25.

Characterisation

The crystalline structures of these catalysts were identified using a Bruker Advance D8 X-ray powder diffractometer (XRD) with Cu Kα radiation (λ–1.5418 Å) at 2θ angle ranging from 20º to 85º with the step size is 0.0260. The phases were determined with the assistance of Joint Committee on Power Diffraction Standard (JCPDS) files. The functional groups of the catalysts were determined using FTIR spectroscopy (Perkin Elmer Spectrum GX FTIR Spectrometer) with IR absorbance data obtained from 400 to 4000 cm^{-1}. The diffuse reflectance analysis of each catalyst was done using UV–Vis DRS (Perkin Elmer Lambda 900) spectrophotometer at room temperature with wavelength between 200 to 600 nm. The photochemical properties, optical and electronic structure of each catalyst were determined using photoluminescence (PL) (JASCO Spectrofluorometer) (FP-8500) with 150W Xe lamp as the excitation source. The textural properties of each catalyst were examined via nitrogen adsorption–desorption isotherms at liquid nitrogen temperatures using a SA 3100 Surface Analyzer (Beckman Coulter) along with Brunnauer-Emmett-Teller (BET) to measure surface area of the catalyst. The surface morphology for each catalyst was confirmed by field-emission scanning electron microscopy (FESEM, JEOLJSM-6701F). The best catalyst was further examined using transmission electron microscopy (TEM, JEOLJEM-2100F). X-ray photoelectron spectroscopy (XPS) was performed on a Kratos Ultra spectrometer equipped with an Mg Kα radiation source (10 mA, 15 kV) to identify the chemical oxidation state of the best catalyst. As reported in the previous work, pH_{ZPC} of each catalyst was determined using powder addition (PA) procedure (Jusoh et al. 2013). 40 mL of pH solution (pH 3, 5, 7, 9 and 11) were prepared with the usage of HCl and NaOH to adjust the pH. The initial pH (pH_i) of each solution was measured prior to addition of the catalyst. After stirring continuously for 48 h, the final pH (pH_f) was taken and the graph of pH_Δ against pH_i was plotted.

Photodegradation of 2-chlorophenol

The photoactivity of these catalysts were tested upon degradation of 2-CP. The photocatalytic reactions were done in a batch reactor with cooling system which connected to 36 W of fluorescence lamp as a visible light source. The average light intensity was 4900 lx. Firstly, 0.375 g L^{-1} of the catalyst was added into 200 mL of 2-CP solution (pH 5, 70 mg L^{-1}) and stirred for 1.5 h in the dark condition to achieve adsorption–desorption equilibrium before continued for another 6.5 h under visible light irradiation. During the reaction, 2 mL of solution were taken out at intervals of 30 min and centrifuged in microcentrifuge at 15,000 rpm for 15 min before being analysed by UV-Vis spectrophotometry (Shimadzu UV-Vis Spectrometer, UV-2600) for determination of residual concentration of the solution. Each set of experiments was performed for triplicates. The adsorption band of 2-CP was measured at 274 nm. The percentage degradation was calculated using the following equation:

$$\text{Degradation}(\%) = \frac{C_0 - C_t}{C_0} \times 100 \quad (1)$$

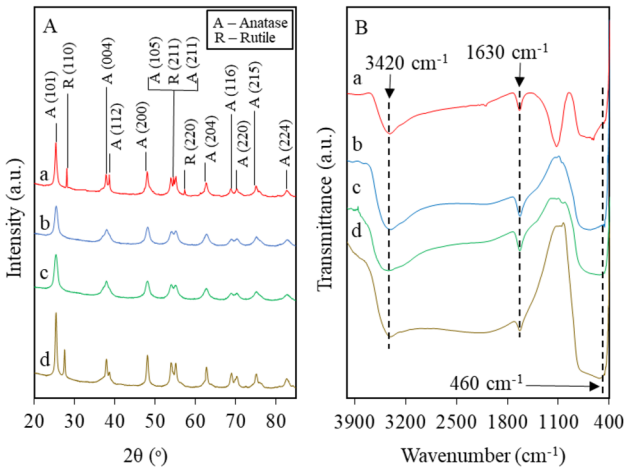

Fig. 1 **A** X-ray diffraction patterns and **B** FTIR spectra of **a** MTN-A **b** MTN-C **c** MTN-NI and **d** P25

where C_0 and C_t are the initial concentration and the concentration at time of 2-CP, respectively.

Results and discussion

Catalysts characterisation

Figure 1A shows the XRD patterns of MTN synthesised under different surfactants and compared with the pretreated commercial TiO_2, Degussa P25. A series of characteristic peaks were observed for MTN and P25 at 25.33°, 37.81°, 38.62°, 48.07°, 53.94°, 55.16°, 62.70°, 68.79°, 70.29°, 75.04° and 82.74° which corresponded to (101), (004), (112), (200), (105), (211), (204), (116), (220), (215) and (224) planes, respectively which consistent with typical peaks of TiO_2 anatase (A) (Jaafar et al. 2015a, b; Rahman et al. 2019). While a series of XRD peaks for rutile (R) phase were observed for MTN-A (Fig. 1A/a) and P25 (Fig. 1A/d) at 28.05°, 54.57° and 57.37° which corresponded to (110), (211) and (220) planes, respectively. No peak associated with TiO_2 brookite was detected (Tzikalos et al. 2012; Sun et al. 2014).

Based on the XRD patterns, MTN-A exhibited the sharpest peaks compared to other catalysts which confirmed the formation of high crystalline structures (Rahman et al. 2019; Hernandez et al. 2022). However, there is a slight difference between the catalysts in terms of structural arrangement due to the dispersion diversity of TiO_2 resulting from the application of different surfactants during the synthesis (Casino et al. 2014; Pal et al. 2016). Besides, the high degree of crystallinity shown by MTN-A benefited from the implementation of anionic surfactants and good heat distribution during the microwave heating with high and instant power density. During the microwave heating, the high microwave field could speedily increase the temperature when it interacts directly with the molecules of the precursor solution (Jaafar et al. 2015a, b).

The XRD results also demonstrated that MTN-C (Fig. 1A/b) and MTN-NI (Fig. 1A/c) only consist of anatase phase while MTN-A (Fig. 1A/a) and P25 (Fig. 1A/d) were mainly composed of anatase and rutile phase. This probably since both cationic and nonionic surfactants were good in maintaining the anatase phase and stabilised this polymorph during the precipitation (Geramipour and Oveisi 2016; Padmanabhan et al. 2018). However, the presence of sodium counterions in sodium dodecyl sulfate (SDS) during the synthesis of MTN-A (Fig. 1A/a) play an important role to assist the phase transition within the catalyst lattice structures (Inada et al. 2009; Hanaor and Sorrell 2011; Darkins et al. 2013; Chaturvedi et al. 2017; Yuenyongsuwana et al. 2018; Prathyusha and Sreenivasan 2020). The phase compositions of MTN-A and P25 were calculated using this equation:

$$\text{Anatase}(\%) = \frac{100}{(1 + I_R/0.79I_A)} \quad (2)$$

where I_R and I_A are the main peaks intensity of anatase (101) and rutile (110), respectively (Ibrahim et al. 2017). MTN-A structures were consisted of 20% rutile and 80% anatase phase while P25 had structures of 21% rutile and 79% anatase. There was only a small difference in phase composition between the mixed-phase catalysts.

In addition, MTN-A (Fig. 1A/a) exhibited the highest peak intensity and containing TiO_2 mixed-phase proved that MTN-A (Fig. 1A/a) has the highest degree of crystallinity compared to other catalysts (Darkins et al. 2013; Chaturvedi et al. 2017; Yuenyongsuwana et al. 2018). The crystallite size of the catalysts was calculated using Debye–Scherrer equation:

$$D = \frac{k\lambda}{\beta\cos\theta} \quad (3)$$

where D is the crystallite size, λ is the wavelength of the X-ray radiation (Cu $K_\alpha = 0.1542$ nm), k is the shape factor

Table 1 Crystallite size and band gap of photocatalysts

Catalyst	[a]Crystallite size (nm)	[b]Band gap (eV)
MTN-A	8.09	3.20
MTN-C	2.36	3.20
MTN-NI	1.77	3.20
P25	4.72	3.10

[a]Crystallite size calculated by using Debye–Scherrer equation at $2\theta = 25.32°$

[b]Band gap calculated by using Kubelka-Munk (K-M) spectrum

($k = 0.94$), β is the line width at half-maximum height, and θ is the angular position of the peak maximum, $2\theta = 25.32°$. As shown in Table 1, the application of different surfactants during the synthesis affects the crystallite's size due to different templates that affect the crystal structures. MTN-A (Fig. 1A/a) have formed the biggest crystallite size followed by P25 (Fig. 1A/d), MTN-C (Fig. 1A/b) and MTN-NI (Fig. 1A/c). The results illustrated that the catalysts with mixed-phase appeared to have relatively bigger crystallite size compared to single phase catalysts (Pijarn et al. 2013; Li et al. 2015; Faisal et al. 2018).

Basically, electrostatic interaction of the polar groups in the surfactant and steric hindrance from the reaction of interfacial energy between the particles have inhibited aggregation, thus maintaining the small crystallite size. Besides, it was reported that cationic and nonionic surfactants formed relatively smaller nanoparticles compared to anionic surfactants. The cations in cationic surfactant attached to the negatively charged Ti-O^- bonds and highly reduced their surface energy which stabilised the nanoparticles in the precursor solution. Therefore, CTAB is an effective surfactant to synthesize uniform spherical TiO_2 nanoparticles with small crystallite size. Nonionic surfactant also produced catalysts with uniform and small crystallite size due to the static repulsion. In contrast, the anions in anionic surfactant (SDS) have induced the micelles to assemble, thus forming irregular spherical nanoparticles (Wei et al. 2018).

The chemical properties of these catalysts were confirmed by FT-IR spectra in the range of 4000–400 cm^{-1} as shown in Fig. 1B. All catalysts showed moderate bands at 3420 and 1630 cm^{-1} which were assigned to the O-H stretching and OH vibration of the surface-adsorbed water, respectively. The presence of surface hydroxyl groups on the catalysts surface could help to enhance their photoactivity (Saravanan et al. 2013b; Mazinani et al. 2014; Gudimella et al.2022). While the band at 460 cm^{-1} were assigned to Ti-O-Ti vibration modes (Jaafar et al. 2017).

The optical properties of each catalyst were investigated by UV-Vis DRS as shown in Fig. 2A. All catalysts illustrated the absorption in the UV region with a band edge around 350 nm and there is no obvious band shift although all the catalysts are particularly different in crystallite. The band gap energy of the catalyst was calculated using the following equation:

$$eV = \frac{hc}{\lambda} \tag{4}$$

where h is Planck's constant (6.626×10^{-3} m^2 kg/s), c is speed of light (3.000×10^8 m/s) and λ is the wavelength values corresponding to the intersection point of the vertical and horizontal parts of the spectra. As shown in Table 1, band gap energy of the MTNs is same value which was 3.2 eV. According to Ravishankar et al. (2020), addition of surfactant during the TiO_2 nanoparticles synthesis did not certainly contribute in lowering the band gap since its only acted as template for the pore formation. Literally, the band gap could be lowered by the formation of lattice defects on the catalyst.

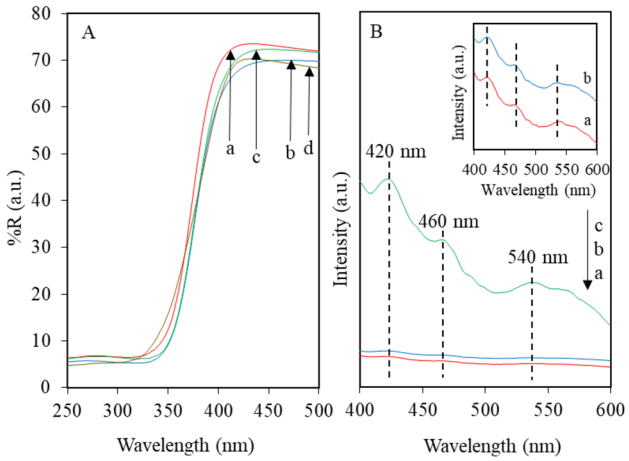

Fig. 2 **A** UV-Vis spectra of **a** MTN-A **b** MTN-C **c** MTN-NI and **d** P25; and **B** PL spectra of **a** MTN-A **b** MTN-C **c** MTN-NI. Insert figure shows the PL spectra of **a** MTN-A and **b** MTN-C

The recombination rate of the photogenerated charge carriers for each catalyst was studied by PL. Figure 2B illustrated the PL spectra for MTNs under the excitation wavelength of 328 nm. The band at 420 nm was corresponding to the surface recombination transition while the bands at 460 nm and 540 nm were attributed to the OV (Jaafar et al. 2015a). Based on the result, MTN-A (Fig. 2B/a and insert Fig. 2B/a) showed the lowest overall intensity followed by MTN-C (Fig. 2B/b and insert Fig. 2B/b) that indicated the catalysts had low recombination rate of the photogenerated charge carriers. Most probably due to the abundance of TSD and OV which acted as electron traps and helped to boost the photoactivity of the catalysts (Pan et al. 2013; Wang et al. 2015a). This will lead to the amount of positively charged holes (h^+) in the valence band were increased and have promoted the production of more hydroxyl radicals (•OH) (Meksi et al. 2015). In contrast, MTN-NI (Fig. 2B/c) manifested the highest overall intensity which reflected that the catalyst had a high recombination rate of the photogenerated charge carriers (Su et al. 2011).

Figure 3A exhibits the nitrogen adsorption–desorption isotherm of the catalysts. All catalysts showed isotherm type V with a H3 hysteresis loop that confirmed the typical adsorption profile for mesostructured material with slit-shaped pores that were non-uniform in size (Wang et al. 2015b, 2016). The hysteresis loop at $P/P_0 = 0.50–0.99$ was assigned to the nitrogen condensation within the void of adjacent nanoparticles which were formed due to textural porosity between the particles (Karim et al. 2014).

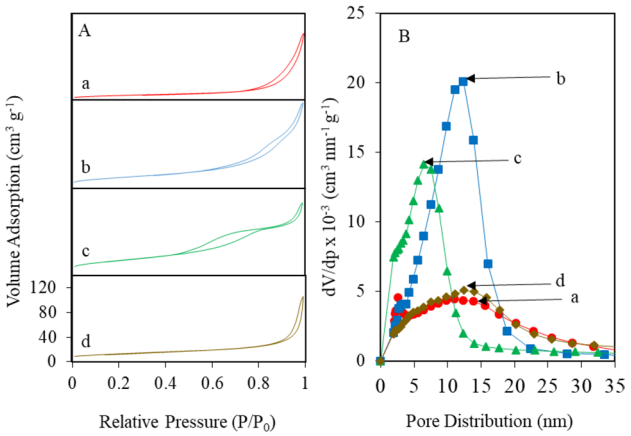

Fig. 3 **A** Nitrogen adsorption–desorption isotherms and **B** Pore distribution of **a** MTN-A **b** MTN-C **c** MTN-NI and **d** P25

Figure 3B demonstrates Barrett-Joyner-Halenda (BJH) pore size distribution of the catalysts. It was observed that the catalysts manifested pores size distribution with different major peaks as shown in Table 2. This result confirmed that all catalysts possessed mesopores on their surface because the pores were less than 50 nm (Bagheri et al. 2015). This probably due to the role of surfactant specifically forming the micelles which functioned as soft templates to help in forming mesopores to increase the surface area (Ramimoghadam et al. 2012; Smirnova et al. 2017). Different surfactants came out with varied micelles size which eventually resulted in dissimilar pores size on the catalysts besides the pores size also affected by the length of the hydrocarbon chains of the surfactant (Hao et al. 2016; Saavedra et al. 2017). Among them, cationic surfactants possessed the longest hydrocarbon chains followed by nonionic and anionic surfactants (Pascual et al. 2018). Thus, MTN-C (Fig. 3B/b) had the largest pores size compared to MTN-A (Fig. 3B/a) and MTN-NI (Fig. 3B/c).

Table 2 reveals the comparison of surface area and pore parameters for each catalyst. MTN-A appeared to have the lowest surface area, total pore volume, and mesoporous volume compared to other catalysts. MTN-A and P25 also displayed negligible quantities of micropores while MTN-C and MTN-NI do not have any micropores on the catalysts surface (Dong et al. 2009; Shouman and Fathy 2018).

The morphologies of the catalysts were further confirmed via FESEM and TEM as shown in Fig. 4. Based on the FESEM images in Fig. 4A-C, all MTNs seemed to have spherical particles with worm hole like surfaces which were non-uniform in shape and size. It was also revealed that all catalysts possessed numerous mesopores. The amount and size of pores in each catalyst were highly dependent on the type of surfactant applied during the synthesis. According to Sun et al. (2014), anionic surfactant is commonly employed to construct nanosized crystal structures that are highly porous which could enhance the photocatalytic activities. While cationic surfactant normally utilised to form grain size particles with pure anatase phase which could greatly improve the surface area (Payormhorm et al. 2017). In contrast, nonionic surfactant usually used to produce macro-/mesoporous structures which promoted good mass transport,

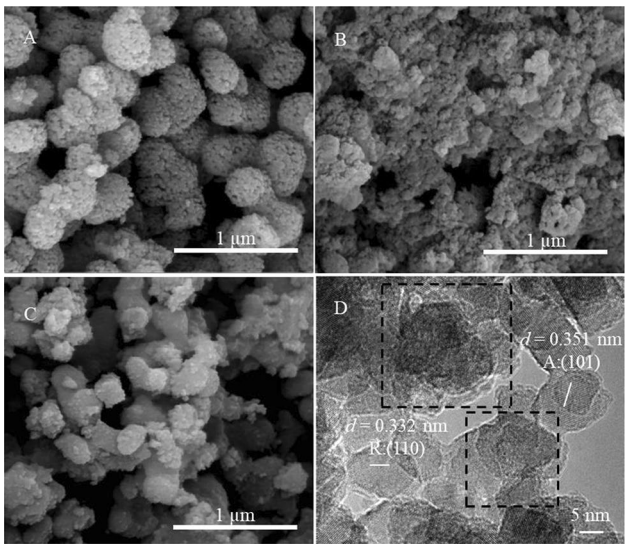

Fig. 4 FESEM images of **A** MTN-A **B** MTN-C **C** MTN-NI and **D** TEM image of MTN-A

Table 2 Textural analysis of photocatalysts

Catalyst	Major peak (nm)	Surface area ($m^2\ g^{-1}$)	[a]Microporous volume ($\times 10^{-3}\ cm^3\ g^{-1}$)	[b]Mesoporous volume ($cm^3\ g^{-1}$)	Total pore volume ($cm^3\ g^{-1}$)
MTN-A	2.55 and 11.06	48.63	2.180	0.114	0.116
MTN-C	12.37	73.55	0.000	0.207	0.207
MTN-NI	6.44	74.98	0.000	0.156	0.156
P25	2.45 and 12.39	42.23	1.264	0.1317	0.133

[a]Microporous volume determined by using *t-plot* method

[b]Mesoporous volume calculated by using this formula: Total pore volume—Microporous volume

constricted channels and built more reachable surface area within the materials (Samsudin et al. 2015).

Figure 4D presents a TEM image of MTN-A which showed the particles were translucent and irregular in shape. Some aggregations (square box) also could be spotted on the catalyst surface resulting from the pores and small particles formed in the catalyst framework. It can also be observed there were two single crystal grains overlapped on each other along with similar interplanar distance of 0.351 nm which was in line with (101) facet in TiO_2 anatase structures. Other than that, the interplanar distance of 0.332 nm was confirmed which is in line with {110} facet in TiO_2 rutile structure. The presence of lattice fringe also proved that high crystalline particles were successfully formed in this catalyst (Rahman et al. 2019).

The chemical states of MTNs synthesised with various surfactants were determined by XPS as illustrated in Fig. 5. Figure 5A reveals the XPS spectra of Ti 2p with Gaussian fits for all MTN in the region of 456–468 eV. The Ti 2p spectrum for MTN-A (Fig. 5A/a) could be fixed into four peaks where the peaks at 458.80 (Ti $2p_{3/2}$), 462.76 (Ti $2p_{1/2}$) and 464.40 (Ti $2p_{1/2}$) eV were attributed to Ti^{3+} site defects (TSD), while the peak at 460.00 (Ti $2p_{3/2}$) eV was assigned to Ti^{4+}. The MTN-C (Fig. 5A/b) illustrated the peaks at 458.80 (Ti $2p_{3/2}$) and 464.40 (Ti $2p_{1/2}$) eV were corresponded to TSD, whereas peaks at 458.40 (Ti $2p_{3/2}$), 460.00 (Ti $2p_{3/2}$) and 464.65 (Ti $2p_{1/2}$) eV were attributed to Ti^{4+}. While the Ti 2p spectrum of MTN-NI (Fig. 5A/c) could be deconvoluted into several peaks where the peak at 464.35 (Ti $2p_{1/2}$) eV was attributed to TSD, while the peaks at 458.35 (Ti $2p_{3/2}$), 460.00 (Ti $2p_{1/2}$) and 464.60 (Ti $2p_{1/2}$) eV were corresponded to Ti^{4+} (Kakavandi et al. 2013; Khan et al. 2014; Vasilopoulou 2014).

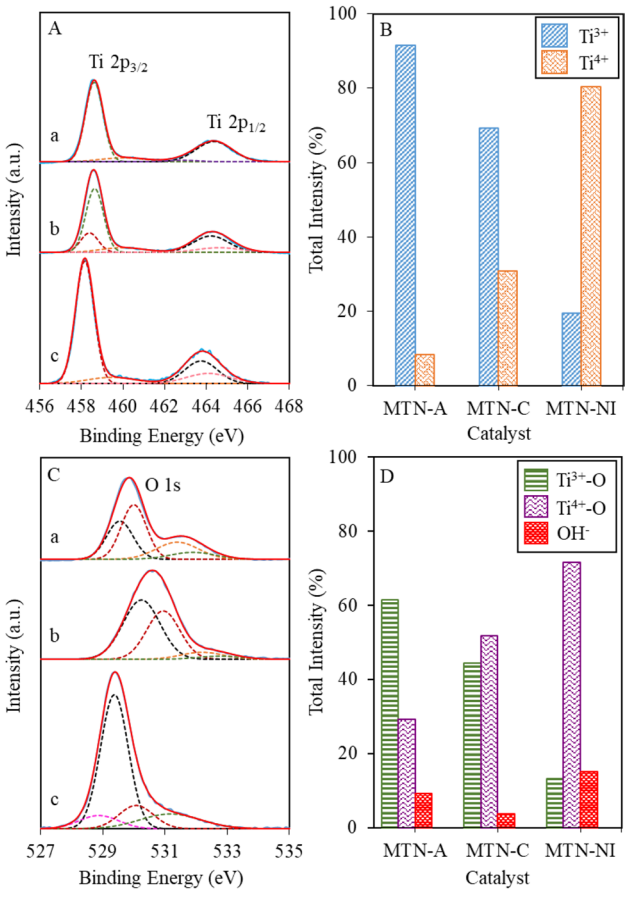

Fig. 5 **A** XPS spectra of Ti 2p; **B** Total intensity of Ti^{3+} and Ti^{4+}; **C** XPS spectra of O 1 s **D** Total intensity of Ti^{3+}-O, Ti^{4+}-O and OH^- of **a** MTN-A **b** MTN-C and **c** MTN-NI

The total intensities of the deconvoluted peaks in Fig. 5A were summaries and compared in Fig. 5B. The results show that MTN-A had the highest amount of TSD compared to MTN-C and MTN-NI. However, MTN-NI appeared to have the highest amount of Ti^{4+} compared to other catalysts which revealed that only small amounts of Ti^{4+} in TiO_2 starting material have been successfully converted into TSD (Ruzicka et al. 2014; Navarrete et al. 2020).

Figure 5C illustrates the XPS spectra of O 1 s with deconvoluted peaks for all catalysts in the region of 527 to 535 eV. The O 1 s spectrum of MTN-A (Fig. 5C/a) proved the presence of oxygen vacancy (OV) or Ti^{3+}-O peaks at 530.00 and 531.40 eV, while Ti^{4+}-O and hydroxide or hydroxyl group (OH^-) peaks at 529.55 and 531.85 eV, respectively. The peaks at 530.80 and 531.70 eV for MTN-C (Fig. 5C/b) were attributed to OV, whereas the peaks at 529.90 and 531.90 eV were assigned to Ti^{4+}-O and hydroxide. The O 1 s spectrum for MTN-NI (Fig. 5C/c) could be fixed into four peaks where the peaks at 530.00 eV was corresponded to OV, 529.20 and 529.45 eV were assigned to Ti^{4+}-O, while 531.60 eV was attributed to hydroxide (Huang et al. 2010; Vasilopoulou 2014).

The total intensities of the deconvoluted peaks in Fig. 5C were summaries and compared in Fig. 5D. The results demonstrated that MTN-A had the highest amount of OV compared to MTN-C and MTN-NI. In contrast, MTN-NI illustrated the highest percentage of Ti^{4+}-O compared to other catalysts which verified the low conversion of lattice oxygen (Ti^{4+}-O) from TiO_2 precursor into OV. All catalysts also presented relatively low percentages of hydroxide (Gharagozlou and Bayati 2014; Li et al. 2014a). Based on the relative intensity of deconvoluted XPS peaks, it was proven that MTN-A has the highest amount of TSD and OV compared to other catalysts.

Basically, different surfactants have different size of micelles, rate of hydrolysis for precursor and rate of growth for nuclei which depend on their alkyl chains. This phenomenon has led to the formation of catalysts with varied crystallite size and pores size. The length and type of alkyl chain also could affect the surface charge density of the micelles. Therefore, increase in the rate of micellisation as the length

of alkyl chain on the polar head group decreased due to the reduction in hydrophobic nature of the molecules (Sheikhnejad-Bishe et al. 2014; Islam and Rankin 2016; Yuan et al. 2016; Shayesteh et al. 2021).

In this study, it was confirmed that counterion of the surfactant played a crucial role during the synthesis of MTN by promoting good structural arrangement with numerous site defects on the catalyst surface. Characterisation results revealed that different surfactants have resulted in different amounts of site defects and phase purity in the structures of the catalysts (Andronic et al. 2011; Hao et al. 2019; Jaafar et al. 2019a; Merin et al. 2020). Previous studies have shown that the phase of the catalyst could be predetermined by altering the pH of the solution (Yuan et al. 2016; Szekely et al. 2019). However, by simply adding the surfactant into the solution also could perform the same task to predetermine the phase of the catalyst besides significantly improving other aspects as well.

Figure 6A–C showed the proposed mechanisms for the formation of TiO_2 phase and site defects for each catalyst. Three important steps during the synthesis which were hydrolysis, microwave heating and calcination really affected the MTN properties. TiO_2 dispersion and structure ordering occurred during hydrolysis process while the implementation of microwave heating step could promote the formation of mesoporous structures with high number of site defects. This was due to the high microwave power density allocated to adequate aging, thus assisting the formation of Ti-O-Ti bonds and hydroxyl groups in the tetrahedral structures. High power density also offered effective condensation where it could eliminate surface oxygen to generate OV while the electrons would be generated to form TSD (Genuino et al. 2012; Jaafar et al. 2015a, 2019a, 2020).

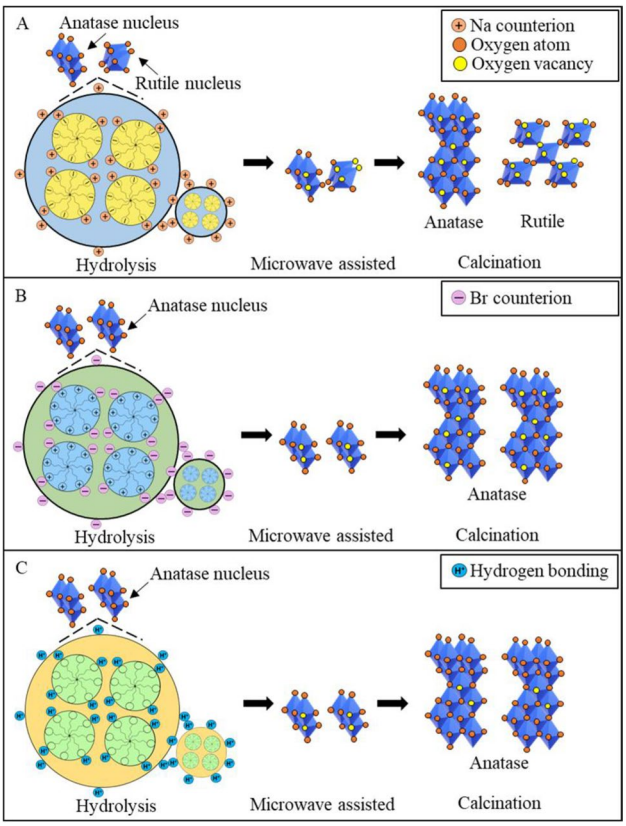

Fig. 6 Proposed mechanism for the formation of TiO_2 phase, TSD and OV in **A** MTN-A **B** MTN-C and **C** MTN-NI

During the calcination process, two important reactions took place which were partially transformation from anatase to rutile and the continuation of TSD and OV formation in the catalysts besides template removal, improved degree of crystallisation, controlled grain growth and formation of mesopores (Majumder et al. 2018; Al-Hajji et al. 2020; He et al. 2020). Commonly, surfactants were fully removed at temperature between 373 to 673K while anatase started to transform into rutile at temperature between 773 to 873K (Cai et al. 2016; Banjuraizah et al. 2018; Ravishankar et al. 2020).

Figure 6A exhibited the proposed mechanism for the formation of mixed-phase MTN-A, TSD and OV. The sodium counterions in SDS promoted the phase transformation which led to the formation of mixed-phase in MTN-A. Sodium counterions began to form the anatase and rutile nucleus during the hydrolysis (Inada et al. 2009; Hanaor and Sorrell 2011; Darkins et al. 2013; Chaturvedi et al. 2017; Prathyusha and Sreenivasan 2020). The mesoporous structures, TSD and OV, started to form during the microwave heating (Jaafar et al. 2015b). After the calcination, anatase and rutile phase were fully formed with the highest amount of TSD and OV on the catalyst surface. This phenomenon could be occurred due to the dispersion of site defects on the rutile surface were better than anatase because the required energy for formation of site defects on the rutile surface were lower compared to anatase. The withdrawal of first and second oxygen atoms from rutile required less energy than anatase which resulted in high number of sites defects on the rutile surface. Recent studies have verified that lower number of site defects were found in anatase compared to rutile, besides the site defects were distributed heterogeneously in rutile and homogenously in anatase of bulk TiO_2 (Fronzi et al. 2016; Wei et al. 2017; Elahifard et al. 2020; Wang et al. 2021).

Figure 6B presented the proposed mechanism for the formation of pure anatase MTN-C, TSD and OV. The bromide counterions in CTAB delayed the phase transition from anatase to rutile and stabilised the anatase phase during the precipitation. Thus, only anatase nucleus were formed during the hydrolysis (Casino et al. 2014). The mesoporous structures, TSD and OV were continued to form during the microwave heating and calcination steps (Jaafar et al. 2019a). As confirmed by the XRD and XPS results, pure

anatase MTN-C had abundant of TSD and OV on the catalyst surface. However, the number of site defects in MTN-C was lower than MTN-A. Even though MTN-C produced a good amount of TSD and OV, the application of cationic surfactant during the synthesis has limited its potential to become a mixed-phase catalyst due to its chemical properties which inhibited the phase transition of the catalyst (Anaam et al. 2019; Dong et al. 2020b).

Figure 6C manifested the proposed mechanism for the formation of pure anatase MTN-NI, TSD and OV. F127 was not ionise in aqueous solution although they had the hydrophilic parts yet still produced anatase nucleus during the hydrolysis (Mohamed and Zak 2020; Rad et al. 2020; Simon et al. 2020). The mesoporous structures, TSD and OV were initiated during the microwave heating (Jaafar et al. 2020). However, the application of high calcination temperature during synthesis of MTN-NI caused the formation of lowest amount for TSD and OV because the optimum calcination temperature for removal of nonionic surfactant was usually around 573K in order to perfectly form mesoporous structures. The calcination temperature for nonionic surfactants were relatively lower compared to other surfactants (Islam et al. 2016; Dong et al. 2017; Marco-Brown et al. 2017). Nonetheless, it was observed in FESEM image for MTN-NI that the pores and crystal structures were fully constructed but the intensity of site defects was found to be very low which indicated the TSD and OV failed to form during synthesis. Previous studies also found that the implementation of high calcination temperature on nonionic surfactant tended to destruct the mesoporous structures progressively which eventually obstructed the formation of site defects on the catalyst surface (Mahoney and Koodali 2014; Wahyuningsih et al. 2014; Nagpure et al. 2018; Kim et al. 2019). All the catalytic properties illustrated the potential of MTN-A to be utilised as a photocatalyst.

Photocatalytic performance of the catalyst

A comparison study on photodegradation of 2-CP compounds using various photocatalysts was summarised in **Table 3**. It shows that MTN-A in this study was comparable with other photocatalysts from other studies. In addition, the synergistic effect between the TSD, OV and mixed-phase MTN have enhanced the electronic band structure, assisted the electron transfer and lowered the electron–hole recombination rate besides increased the photoactivity under wider light range.

The catalytic performances of MTNs prepared by different surfactants were tested on degradation of 2-CP under dark and visible light irradiation as shown in Fig. 7. All catalysts still showed low percentage degradation under dark condition due to the adsorption of 2-CP to the mesopores. It was also clearly observed that all the catalysts showed better performance under visible light irradiation compared to being in dark. Thus, it was confirmed that 2-CP removal was due to the photocatalytic degradation rather than adsorption.

Photocatalytic degradation with MTN-A demonstrated the highest percentage degradation (85%) followed by MTN-C (77%), P25 (62%) and MTN-NI (18%), signifying the importance of mixed-phase of TiO_2 in the system.

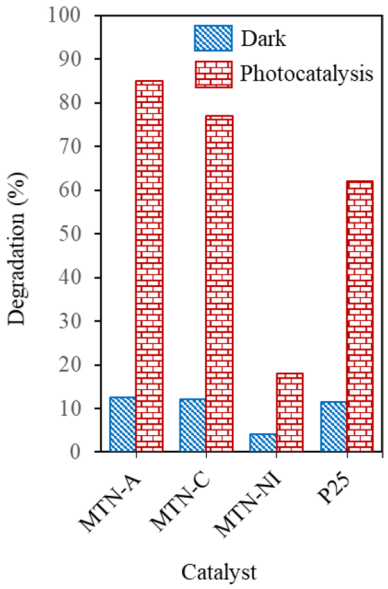

Fig. 7 Photocatalytic performance of MTN-A, MTN-C, MTN-NI and P25. ($C_{2\text{-CP}}$ = 70 mg L^{-1}, pH = 5, W = 0.375 g L^{-1}, t = 8 h, T = 303 K)

Table 3 Comparison of 2-chlorophenol degradation over various catalysts

Catalyst	Initial conc (mg L^{-1})	Dosage (g L^{-1})	Degradation (%)	Refs.
Iodine doped TiO_2 modified with SnO_2 (SIT)	30	1.000	88	He et al. 2011
Ga,I-TiO_2	32	1.000	90.0	Song et al. 2011
$InVo_4/TiO_2$	50	1.000	50.5	Rashid et al. 2014
Ag/TiO_2	50	0.375	94.0	Jaafar et al., 2015a
(RGO)-(TIO_2-RGO-CoO)	10	2.000	98.2	Sharma and Lee 2016
Fe_3O_4-TiO_2@MWCNT	2	0.400	100.0	Dobaradaran et al. 2018

Regardless of all catalysts had the same band gap energy, MTN-A still illustrated an excellent performance contributed to the numerous amounts of TSD and OV on its surface. These site defects created new bands within the electronic band structure, thus the photoactivity could be extended under visible light irradiation (Wang et al. 2015a; Huang et al. 2020). The presence of site defects and the conduction band (C_B) of rutile in MTN-A could act as electron acceptors by reducing the electron–hole recombination, thus improved the photocatalytic performance. Moreover, the formation of electron–hole pairs under visible light irradiation have escalated due to the excitation of electrons (e^-) from V_B and TSD. In contrast, under UV light irradiation, this occurrence did not happen because UV possessed very high energy besides able to excite electrons directly from V_B to C_B. Therefore, the higher the number of TSD and OV on the catalyst surface could led to high percentage degradation of the pollutant (Pan et al. 2013; Ren et al. 2015).

The pH of solution is an important parameter in photocatalytic degradation because it can regulate the interaction between the pollutant and catalyst surface besides affected the adsorption capacity. It also can control the amount of hydroxyl radical produced during the photocatalytic degradation. In order to identify the optimal pH for MTN-A in photodegradation of 2-CP, the pH values of the aqueous solution were altered from 3 to 11. The selection of pH was done based on the optimum condition reported by the previous studies (Dobaradaran et al. 2018; Barakat et al. 2020).

Figure 8A shows the highest degradation was obtained in pH 5 with percentage degradation of 85% while followed by pH 3, 7, 9 and 11 with percentage degradation of 45%, 40%, 20% and 16%, respectively. This phenomenon could be clarified by the amphoteric properties of the catalyst in term of Point of Zero Charge (PZC) (Karim et al. 2014). The PZC value of MTN-A was at pH 6 as illustrated in Fig. 8B

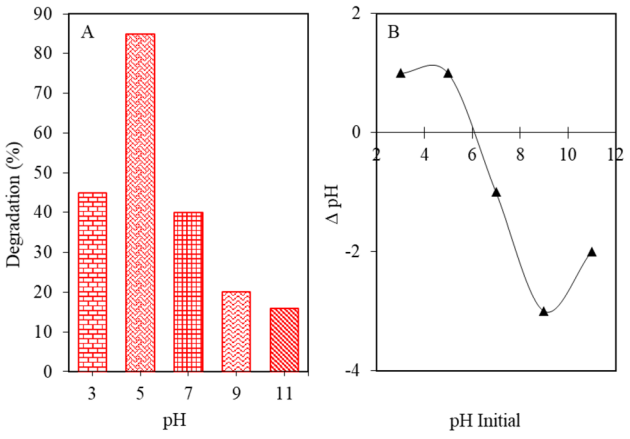

Fig. 8 **A** Effect of pH using MTN-A for degradation of 2-CP and **B** Isoelectric point (pH_{PZC}) of MTN-A. ($C_{2\text{-}CP}$ = 70 mg L^{-1}, W = 0.375 g L^{-1}, t = 8 h, T = 303 K)

while the pKa value of 2-CP is 8.52 (Duan et al. 2021). Below the pK_a value, 2-CP existed in the neutral form and did not exhibit repulsion with the negatively charged MTN-A. Thus, MTN-A manifested optimum photocatalytic degradation in lower pH condition. While above the pK_a value, 2-CP became negatively charged ions and repulsed with the negatively charged MTN-A. Moreover, high pH values favored the formation of carbonate ions which functioned as scavenger for hydroxyl radicals. Therefore, decreased in percentage degradation was observed at higher pH.

Figure 9A displays the photocatalytic performance of MTN-A at various initial concentration of 2-CP. It was revealed that MTN-A successfully degraded 70 mg L^{-1} of 2-CP with 85% degradation followed by 100 mg L^{-1} (82%), 50 mg L^{-1} (71%), 30 mg L^{-1} (66%) and 10 mg L^{-1} (50%). The trend of this result exhibited that better photoactivity were achieved in pollutants with higher initial concentration whereas lesser photodegradation were obtained in pollutants with lower initial concentration. The adsorption capacity influenced by the availability of adsorption sites on MTN-A. At low initial concentration, the proportion of 2-CP molecules to the amount of unoccupied adsorption sites was low which signified less competition for the adsorption sites. The rate of mass transfer increased and adsorption took place progressively. Therefore, the percentage degradation increased from 10 to 50 mg L^{-1}. Then, the initial concentration continued to increase until the maximum adsorption capacity was reached at 70 mg L^{-1}. On the other hand, at high initial concentration, the proportion of 2-CP molecules to the amount of unoccupied adsorption sites was high which indicated high competition for the adsorption sites. Excess 2-CP molecules were not adsorbed because of the electrostatic repulsion, thus decreased the adsorption capacity.

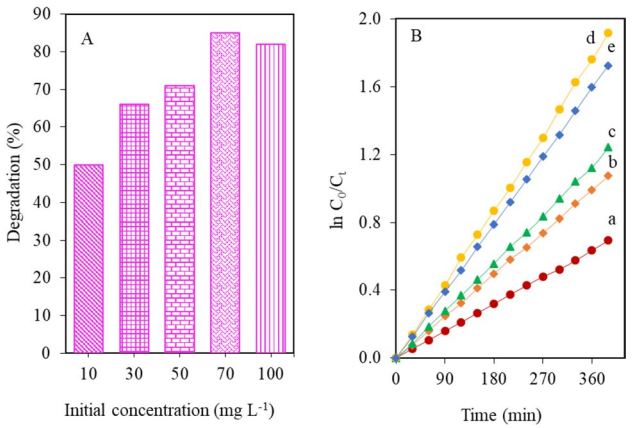

Fig. 9 **A** Effect of initial concentration using MTN-A for degradation of 2-CP and **B** Photodegradation kinetics of 2-CP using MTN-A at different initial concentrations **a** 10 mg L^{-1} **b** 30 mg L^{-1} **c** 50 mg L^{-1} **d** 70 mg L^{-1} **e** 100 mg L^{-1}. (pH = 5, W = 0.375 g L^{-1}, t = 8 h, T = 303 K)

Table 4 Percentage degradation at different initial concentrations of 2-CP and pseudo-first order apparent constant values for 2-CP degradation using MTN-A. (pH = 5, W = 0.375 g L^{-1}, t = 8 h, T = 303K)

Initial 2-CP concentration, C_0	Degradation (%)	Reaction rate, k_{app} ($\times 10^{-2}$ min^{-1})	Initial reaction rate, r_0 (mg L^{-1} min^{-1})
10	50	0.18	0.02
30	66	0.27	0.08
50	71	0.31	0.16
70	85	0.49	0.34
100	82	0.44	0.44

Hence, the percentage degradation started to decrease at 100 mg L^{-1} (Salleh et al. 2011; Yagub et al. 2014).

Figure 9B also demonstrates a graph of ln (C_o/C_t) against the irradiation time for a sequence of initial concentration at 10, 30, 50, 70 and 100 mg L^{-1} which followed the Langmuir–Hinshelwood model (Sapawe et al. 2013a). The kinetic analysis was studied using this model to understand the reactions occurred at solid–liquid interface (Jawad et al. 2016). From the graph plotted, it was proposed that the photocatalytic degradation of 2-CP followed pseudo-first order kinetics model (Jalil et al. 2013). The kinetic study of MTN-A has been studied and the degradation efficiency was summarised in Table 4. The increase of k_{app} values with the increment of initial concentration have suggested that the system was favored at high concentration (Sapawe et al. 2013b). The values of k_r (reaction rate constant) and K_{LH} (adsorption coefficient) for MTN-A were found to be 121.9512 mg L^{-1} min^{-1} and 4.5556 L mg^{-1}, respectively. Since the value of k_r was larger than K_{LH}, it was indicated that the adsorption of 2-CP was the controlling step in the process (Jaafar et al. 2012; Sapawe et al. 2012).

The effect of catalyst dosage was also studied to analyse the efficacy of MTN-A to adsorb 2-CP with minimum mass of catalyst as shown in Fig. 10A. The results show that 0.375 g L^{-1} gave the best photocatalytic performance with percentage degradation of 85% followed by 0.250, 0.125, 0.500 and 0.625 g L^{-1} with percentage degradation of 79%, 77%, 75% and 74%, respectively. As MTN-A dosage increased from 0.250 to 0.375 g L^{-1}, the trend of percentage degradation was increased while the adsorption capacity was decreased due to the high amount of available adsorption sites. However, further increased in catalyst dosage more than 0.375 g L^{-1} have lowered the number of available adsorption sites on the catalyst due to aggregation which reduced the photoactivity besides too high catalyst dosage could cause turbidity of the suspension in the pollutant which restricted the light penetration toward the catalyst surface (Zhou et al. 2014; Shah et al. 2015).

The potential of MTN-A for degradation of chlorophenol derivatives namely phenol, 2-CP, 3-CP, 4-CP and 2,4-DCP

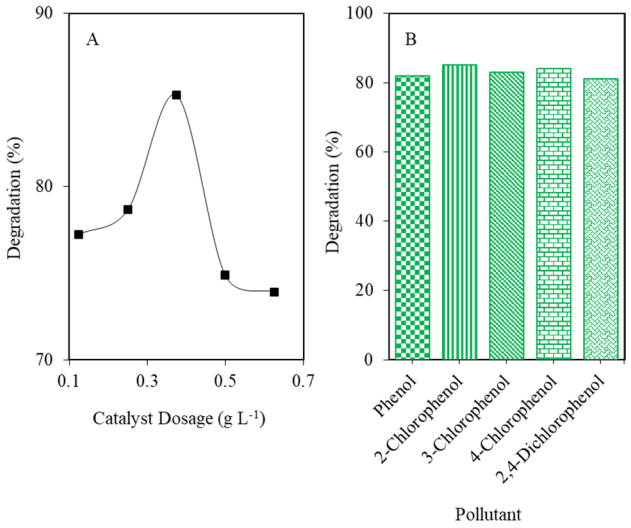

Fig. 10 **A** Effect of catalyst dosage using MTN-A during degradation of 2-CP and **B** Photocatalytic degradation of phenol derivatives. ($C_{2\text{-CP}}$ = 70 mg L^{-1}, pH = 5, W = 0.375 g L^{-1}, t = 8 h, T = 303 K)

was studied as shown in Fig. 10B. All the phenolic derivatives were combined as one solution and labelled simulated phenols. The results demonstrated that the catalyst successfully degraded more than 80% of all pollutants with 2-CP (85%) maintained as the most degraded pollutant followed by 4-CP (84%), 3-CP (83%), phenol (82%) and 2,4-DCP (81%). Since 2-CP showed the highest percentage degradation, thus it was chosen for the optimization study. This result proved that MTN-A could be greatly suitable for industrial treatments which usually contained several chlorophenol derivatives in their wastes water (Munoz et al. 2011; Castaneda et al. 2016; Guo et al. 2021).

The stability of MTN-A is studied by a series of experiment repetition in the photocatalytic degradation of 2-CP as shown in Fig. 11A. MTN-A was collected, washed and calcined at 873K for 3 h for each new cycle. The result shows that photocatalytic performance of the catalyst remained active with only slight decreased in percentage degradation from 85 to 77%. The decreased in degradation probably during the drying process for each cycle, the catalyst exposed to additional heat which contributed in reducing the surface area as well as the catalyst accumulation that led to decrease in photocatalytic degradation of pollutant in the next cycles (Jaafar et al. 2012). Thus, it was proven that MTN-A had great potential to be used at industrial scale since it was very stable and cost effective.

In order to study the photocatalytic degradation mechanism of 2-CP using MTN-A, three scavenging agents were introduced specifically potassium peroxodisulfate (PP), sodium oxalate (SO) and potassium iodide (KI) where PP functioned as e^- trapper, SO acted as h^+ trapper and KI operated as surface hydroxyl radical $^{\bullet}OH$ trapper (Jusoh

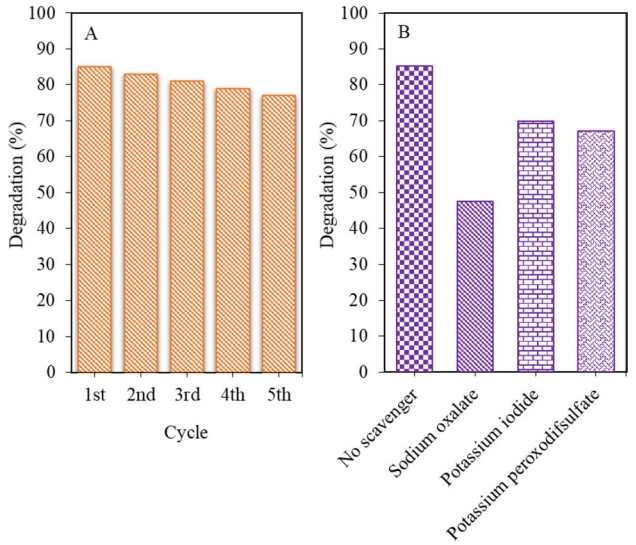

Fig. 11 **A** Regeneration of MTN-A on degradation of 2-CP and **B** Photocatalytic degradation of 2-CP in the presence of hole scavenger, electron scavenger and •OH scavenger using MTN-A. ($C_{2\text{-}CP}$ = 70 mg L^{-1}, pH = 5, W = 0.375 g L^{-1}, t = 8 h, T = 303 K)

et al. 2014). Figure 11B exhibits the percentage degradation of 2-CP after addition of these scavenging agents. The result revealed that additional of KI during the reaction gave the highest percentage degradation of 70% followed by PP and SO with percentage degradation of 67% and 47%, respectively. This result also signified the important role of h^+ during the photocatalytic degradation followed by e^- and •OH.

The proposed mechanism for the degradation of 2-CP over MTN-A is proposed as in Fig. 12 according to the characterisations and photoactivities results. Generally, visible light irradiation triggered the photogenerated electrons to excite from V_B to the C_B that resulted in the production of electron–hole pairs on the MTN-A surface as shown in Eq. 5 (Saravanan et al. 2013a; Nur et al. 2022).

$$TiO_2 + hv \rightarrow TiO_2 + h_{VB} + e_{CB-} \quad (5)$$

The TSD, OV and C_B of rutile assisted the charge migration and inhibited the electron–hole recombination of the MTN-A (Abdullah et al. 2018). The presence of TSD and OV were confirmed with the restricted electrons movement during the photocatalytic degradation due to scavenger effect on the electrons. Then, the generated h^+ in the V_B reacted with the water molecules or hydroxyl groups to generate •OH radicals as illustrated in Eq. 6 and Eq. 7.

$$H_2O + h_{VB} \rightarrow OH + H^+ \quad (6)$$

$$OH^- + h_{VB} \rightarrow OH \quad (7)$$

The photogenerated electrons from different platforms have reduced O_2 molecules into superoxide ($O_2^{\bullet-}$) and then

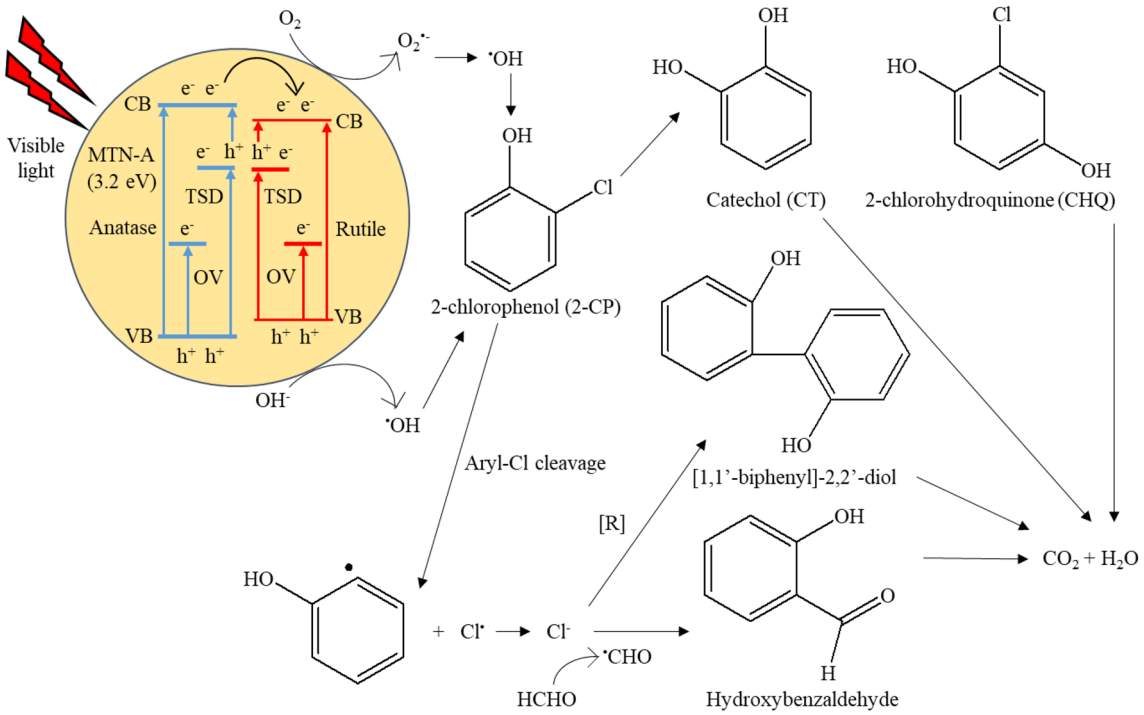

Fig. 12 Proposed mechanism for the degradation of 2-CP using MTN-A

reacted with H^+ in the water to produce $HOO^{\bullet}$ followed by the generation of $^{\bullet}OH$ for partial or complete mineralisation of 2-CP. The more $O_2^{\bullet-}$ production during the photocatalytic activities which further generated the $^{\bullet}OH$, the higher the percentage degradation of 2-CP. Based on the previous study, $^{\bullet}OH$ had electrophilic nature that tended to bombard an aromatic structure. This occurrence has led to the generation of hydroxylated species such as catechol and 2-chlorohydroquinone. Besides, 2-CP might go through hemolytic cleavage of aryl-Cl bond which then produced radical (R) and chloride radical ($Cl^{\bullet}$). The dichlorination of 2-CP possibly occurred via its interaction with trapped electrons on the catalyst surface forming R and chlorine ions. After that, R might distinguish into [1,1'-biphenyl]-2,2'-diol or reacted with formyl radical formed in-situ that generated hydroxybenzaldehyde. Persistent oxidation of the aromatic intermediates might induce ring opening and producing carboxylic acid which caused total mineralisation of 2-CP into CO_2 and H_2O (Jusoh et al. 2015; Jaafar et al. 2020; Marfur et al. 2020b). The mechanism was summarized as in Eqs. 8, 9 and 10.

$$O_2 + e_{CB} \rightarrow O_{2-} \quad (8)$$

$$^{\cdot}O_2^- + H^+ \rightarrow HO_2 \rightarrow OH \quad (9)$$

$$^{\cdot}OH + 2-CP \rightarrow \text{degraded } 2-CP + CO_2 + H_2O \quad (10)$$

This study revealed the remarkable functions of TSD, OV and C_B of rutile in MTN-A which highly contributed to assisting the charge carrier separation and acted as electron acceptors to inhibit the electron–hole recombination. Besides, the optical response was shifted from UV to the visible light region (Bielan et al. 2020; Miao et al. 2020; Xu et al. 2021).

Conclusion

In this study, MTN-A, MTN-C and MTN-NI were synthesised using anionic, cationic and nonionic surfactants, respectively via microwave-assisted method and characterised by XRD, FTIR, UV-Vis DRS, PL, BET, FESEM, TEM and XPS. Then, the photocatalytic activities of the catalysts were tested using degradation of 2-CP under visible light irradiation. MTN-A have showed the highest percentage degradation with 85% followed by MTN-C, MTN-NI and P25 with 77%, 18% and 62%, respectively. Based on the characterisation results, it was revealed that introduction of different surfactants was found to give different structural arrangement and TiO_2 dispersion during the synthesis. All catalysts were successfully formed the mesoporous structures, but this occurrence resulted in different degree of crystallinity, phase composition, pores and particles size of the catalysts structures. The significant difference between the prepared catalysts was the formation of mixed-phase when using SDS as anionic surfactant. MTN-A consisted of 20% rutile and 80% anatase phase. Mixed-phase MTN-A had the highest number of TSD and OV on the catalyst surface compared to other catalysts. This was contributed by the presence of rutile phase in the framework. The amount of site defects on the surface of rutile were higher than anatase because the energy needed for formation of site defect on rutile were lower compared to anatase. Abundance of TSD and OV on the MTN-A surface have resulted in the highest degradation. The synergistic effect between the TSD, OV and TiO_2 mixed-phase have assisted the charge migration and inhibited the electron–hole recombination rate, thus increased the photoactivity of MTN-A. MTN-A also exhibited the highest degree of crystallinity compared to other catalysts. MTN-A was found to work the best with dosage of 0.375 g L^{-1} in solution of pH 5 and 70 mg L^{-1}. The kinetic study for MTN-A indicated that the degradation of 2-CP followed a pseudo-first-order Langmuir–Hinshelwood model. Besides, the employment of MTN-A on the degradation of phenol derivatives such as phenol, 2-CP, 3-CP, 4-CP and 2,4-DCP had also shown significant performance of the catalytic system. The regeneration study of the catalyst exhibited that the photocatalytic activity was still stable after five cycles with only a slight decrease in the degradation of 2-CP. Thus, MTN-A is highly potential to be used at industrial scale since it was very stable against photo- and chemical corrosion even after repeated cycles.

Acknowledgements The authors are grateful for the financial support by Universiti Sains Malaysia (USM) for Short Term Grant (304/PKIMIA/6315610).

Funding This research was supported by Universiti Sains Malaysia (USM) for Short Term Grant (304/PKIMIA/6315610).

Declarations

Conflicts of interest Author N.F. Jaafar has received research grants from Universiti Sains Malaysia (USM) for Short Term Grant.

Ethical approval This article does not contain any studies with human participants or animals performed by any of the authors.

References

Abdullah SA, Sahdan MZ, Nafarizal N, Saim H, Bakri AS, Rohaida CCH, Adriyanto F, Sari Y (2018) Photoluminescence study of trap-state defect on TiO_2 thin films at different substrate temperature via RF magnetron sputtering. J Phys Conf Ser 995:1–8. https://doi.org/10.1088/1742-6596/995/1/012067

Al-Hajji LA, Ismail AA, Al-Hazza A, Ahmed SA, Alsaidi M, Almutawa F, Bumajdad A (2020) Impact of calcination of

hydrothermally synthesized TiO_2 nanowires on their photocatalytic efficiency. J Mol Struct 1200:127153–127164. https://doi.org/10.1016/j.molstruc.2019.127153

Anaam SAA, Saim H, Sahdan MZ, Al-Gheethi A (2019) Defective TiO_2 with intrinsic point defects for photocatalytic hydrogen production: a review. Int J Nanoelectron Mater 12:495–516

Andronic L, Andrasi D, Enesca A, Visa M, Duta A (2011) The influence of titanium dioxide phase composition on dyes photocatalysis. J Sol-Gel Sci Technol 58:201–208. https://doi.org/10.1007/s10971-010-2378-3

Arora N, Gupta M (2022) An experimental analysis of CTAB surfactant on thermo-physical properties and stability of MWCNT/water nanofluids. Appl Nanosci. https://doi.org/10.1007/s13204-022-02458-x

Assayehegn E, Solaiappan A, Chebude Y, Alemayehu E (2020) Fabrication of tunable anatase/rutile heterojunction N/TiO_2 nanophotocatalyst for enhanced visible light degradation activity. Appl Surf Sci 515:145966. https://doi.org/10.1016/j.apsusc.2020.145966

Bagheri S, Julkapli NM (2016) Mixed phase TiO_2 photocatalysis: correlation between phase composition and photodecomposition of water pollutants. Rev Inorg Chem 37:1–18. https://doi.org/10.1515/revic-2016-0001

Bagheri S, Hir ZAM, Yousefi AT, Hamid SBA (2015) Progress on mesoporous titanium dioxide: synthesis, modification and applications. Microporous Mesoporous Mater 218:206–222. https://doi.org/10.1016/j.micromeso.2015.05.028

Banjuraizah J, Ong YP, Ahmad ZA (2018) Effect of calcination temperature on titanium dioxide synthesized by sol-gel method. Int J Curr Sci Eng Technol 1:68–74. https://doi.org/10.30967/ijcrset.1.S1.2018.68-74

Barakat MA, Kumar R, Rashid J, Seliem MK, Al-Mur B, El-Shishtawy RM (2020) A novel CuO-Cu_2O/Ag-Ag_3PO_4 nanocomposite: synthesis, characterization, and its application for 2-chlorophenol decontamination under visible light. J Taiwan Inst Chem Eng 115:208–217. https://doi.org/10.1016/j.jtice.2020.10.030

Bielan Z, Dudziak S, Sulowska A, Pelczarski D, Ryl J, Zielinska-Jurek A (2020) Preparation and characterization of defective TiO_2. The effect of the reaction environment on titanium vacancies formation. Mater 13:2763–2788. https://doi.org/10.3390/ma13122763

Cai J, Xin W, Liu G, Lin D, Zhu D (2016) Effect of calcination temperature on structural properties and photocatalytic activity of Mn-C-codoped TiO_2. Mater Res 19:401–407. https://doi.org/10.1590/1980-5373-MR-2015-0381

Casino S, Lupo FD, Francia C, Tuel A, Bodoardo S, Gerbaldi C (2014) Surfactant-assisted sol gel preparation of high-surface area mesoporous TiO_2 nanocrystalline Li-ion battery anodes. J Alloys Compd 594:114–121. https://doi.org/10.1016/j.jallcom.2014.01.111

Castaneda C, Tzompantzi F, Gomeza R, Rojas H (2016) Enhanced photocatalytic degradation of 4-chlorophenol and 2,4-dichlorophenol on in situ phosphated sol-gel TiO_2. J Chem Technol Biotechnol 91:2170–2178. https://doi.org/10.1002/jctb.4943

Chakhtouna H, Benzeid H, Zari N, Qaiss AEK, Bouhfid R (2021) Recent progress on Ag/TiO_2 photocatalysts: photocatalytic and bactericidal behaviors. Environ Sci Pollut Res 28:44638–44666. https://doi.org/10.1007/s11356-021-14996-y

Chaturvedi A, Joshi MP, Mondal P, Sinha AK, Srivastava AK (2017) Growth of anatase and rutile phase TiO_2 nanoparticles using pulsed laser ablation in liquid: influence of surfactant addition and ablation time variation. Appl Surf Sci 396:303–309. https://doi.org/10.1016/j.apsusc.2016.10.133

Darkins R, Sushko ML, Liu J, Duffy DM (2013) Adhesion of sodium dodecyl sulfate surfactant monolayers with TiO_2 (rutile and anatase) surfaces. Langmuir 29:11609–11614. https://doi.org/10.1021/la401469f

Das P, Bahadur N, Dhawan V (2020) Surfactant-modified titania for cadmium removal and textile effluent treatment together being environmentally safe for seed germination and growth of Vigna radiata. Environ Sci Pollut Res 27:7795–7811. https://doi.org/10.1007/s11356-019-07480-1

Diyuk VE, Zaderko AN, Grishchenko LM, Afonin S, Mariychuk R, Kanuchova M, Lisnyak VV (2022) Preparation, texture and surface chemistry characterization of nanoporous-activated carbons co-doped with fluorine and chlorine. Appl Nanosci. https://doi.org/10.1007/s13204-022-02459-w

Dobaradaran S, Nodehi RN, Yaghmaeian K, Jaafari J, Niari MH, Bharti AK, Agarwal S, Gupta VK, Azari A, Shariatifar N (2018) Catalytic decomposition of 2-chlorophenol using anultrasonic-assisted Fe_3O_4–TiO_2@MWCNT system: Influence factors, pathway and mechanism study. J Colloid Interface Sci 512:172–189. https://doi.org/10.1016/j.jcis.2017.10.015

Dong YR, Nishiyama N, Kodama M, Egashira Y, Ueyama K (2009) Nitrogen-containing microporous carbons prepared from anionic surfactant-melamine/formaldehyde composites. Carbon 47:2138–2141. https://doi.org/10.1016/j.carbon.2009.04.011

Dong W, Yao Y, Li L, Sun Y, Hua W, Zhuang G, Zhou D, Yan S, Song W (2017) Three-dimensional interconnected mesoporous anatase TiO_2 exhibiting unique photocatalytic performances. App Catal B: Environ 217:293–302. https://doi.org/10.1016/j.apcatb.2017.05.083

Dong J, Hu C, Qi W, An X, Liu H, Qu J (2020a) Defect-enhanced photocatalytic removal of dimethylarsinic acid over mixed-phase mesoporous TiO_2. J Environ Sci 91:35–42. https://doi.org/10.1016/j.jes.2019.12.013

Dong Y, Zhang W, Tao Y (2020b) CTAB modified TiO_2 supported on HZSM-5 zeolite for enhanced photocatalytic degradation of azophloxine. J Mater Res Technol 9:9403–9411. https://doi.org/10.1016/j.jmrt.2020.05.091

Duan J, Ji H, Xu T, Pan F, Liu X, Liu W, Zhao D (2021) Simultaneous adsorption of uranium(VI) and 2-chlorophenol by activated carbon fiber supported/modified titanate nanotubes (TNTs/ACF): effectiveness and synergistic effects. Chem Eng J 406:1–12. https://doi.org/10.1016/j.cej.2020.126752

Elahifard M, Sadrian MR, Mirzanejad A, Ardakani RB, Ahmadvand S (2020) Dispersion of defects in TiO_2 semiconductor: oxygen vacancies in the bulk and surface of rutile and anatase. Catal 10:397–407. https://doi.org/10.3390/catal10040397

Faisal M, Harraz FA, Ismail AA, El-Toni AM, Al-Sayari SA, Al-Hajry A, Al-Assiri MS (2018) Novel mesoporous NiO/TiO_2 nanocomposites with enhanced photocatalytic activity under visible light illumination. Ceram Int 44:7047–7056. https://doi.org/10.1016/j.ceramint.2018.01.140

Fronzi M, Daly W, Nolan M (2016) Reactivity of metal oxide nanocluster modified rutile and anatase TiO_2: oxygen vacancy formation and CO_2 interaction. Appl Catal A 521:240–249. https://doi.org/10.1016/j.apcata.2015.11.038

Fu W, Li G, Wang Y, Zeng S, Yan Z, Wang J, Xin S, Zhang L, Wu S, Zhang Z (2018) Facile formation of mesoporous structured mixed-phase (anatase/rutile) TiO_2 with enhanced visible light photocatalytic activity. Chem Commun 54:58–61. https://doi.org/10.1039/c7cc05750d

Genuino HC, Hamal DB, Fu YJ, Suib SL (2012) Synergetic effects of ultraviolet and microwave radiation for enhanced activity of TiO_2 nanoparticles in degrading organic dyes using a continuous-flow reactor. J Phys Chem C 116:14040–14051. https://doi.org/10.1021/jp3040192

Geramipour T, Oveisi H (2016) Microstruture and surface characteristics evolution of mesoporous multiple spin-coated titania film. Thin Solid Films 619:353–358

Gharagozlou M, Bayati R (2014) Photocatalytic activity and formation of oxygen vacancies in cation doped anatase TiO_2 nanoparticles.

Ceram Int 40:10247–10253. https://doi.org/10.1016/j.ceramint.2014.02.114

Gudimella KK, Gedda G, Kumar PS, Babu BK, Yamajala B, Rao BV, Singh PP, Kumar D, Sharma A (2022) Novel synthesis of fluorescent carbon dots from bio-based Carica Papaya Leaves: optical and structural properties with antioxidant and anti-inflammatory activities. Environ Res 204:111854. https://doi.org/10.1016/j.envres.2021.111854

Guo T, Yang S, Chen Y, Yang L, Sun Y, Shang Q (2021) Photocatalytic kinetics and cyclic stability of photocatalysts Fe-complex/TiO_2 in the synergistic degradation of phenolic pollutants and reduction of Cr(VI). Environ Sci Pollut Res 28:12459–12473. https://doi.org/10.1007/s11356-020-11220-1

Hanaor DAH, Sorrell CC (2011) Review of the anatase to rutile phase transformation. J Mater Sci 46:855–874. https://doi.org/10.1007/s10853-010-5113-0

Hao LS, Jia YF, Liu Q, Wang Y, Xu GY, Nan YQ (2016) Influences of molecular structure of the cationic surfactant, additives and medium on the micellization of cationic/anionic surfactant mixed systems. Colloids Surf A Physicochem Eng Aspects 511:91–104. https://doi.org/10.1016/j.colsurfa.2016.09.054

Hao L, Yan J, Guan S, Cheng L, Zhao Q, Zhu Z, Wang Y, Lu Y, Liu J (2019) Oxygen vacancies in TiO_2/SnOx coatings prepared by ball milling followed by calcination and their influence on the photocatalytic activity. Appl Surf Sci 466:490–497. https://doi.org/10.1016/j.apsusc.2018.10.071

He Y, Zhong L, Wang X, He J, Wang L, Zhong C, Liu M, Zhao Y, Lai X, Bi J, Gao D (2020) ZIF-8 derived $ZnWO_4$ nanocrystals: calcination temperature induced evolution of composition and microstructures, and their electrochemical performances as anode for lithium-ion batteries. Electrochim Acta. https://doi.org/10.1016/j.electacta.2020.137435

Hernandez P, Santiago-Cuevas A, Palacios-Cabrera C, Thangarasu P, Narayanan J, Kaur H, Singh J, Kumar D, Huerta-Aguilar CA, Singh PP, Vo D-VN, Sharma A (2022) Development and applications of Ru and Ce based iron oxides as photocatalysts. Mater Lett 313:131720. https://doi.org/10.1016/j.matlet.2022.131720

Huang CN, Bow JS, Zheng Y, Chen SY, Ho N, Shen P (2010) Non-stoichiometric titanium oxides via pulsed laser ablation in water. Nanoscale Res Lett 5:972–985. https://doi.org/10.1007/s11671-010-9591-4

Huang CW, Sin WC, Nguyen VH, Wu YC, Chen WY, Chien AC (2020) Solvothermal synthesis of mesoporous TiO_2 using sodium dodecyl sulfate for photocatalytic degradation of methylene blue. Top Catal 11:1–10. https://doi.org/10.1007/s11244-020-01322-y

Ibrahim A, Mekprasart W, Pecharapa W (2017) Anatase/Rutile TiO_2 composite prepared via sonochemical process and their photocatalytic activity. Mater Today: Proc 4:6159–6165. https://doi.org/10.1016/j.matpr.2017.06.110

Ihnatiuk D, Vorobets V, Sihor M, Tossi C, Kolbasov G, Smirnova N, Tittonen I, Eremenko A, Koci K, Linnik O (2022) Photoelectrochemical, photocatalytic and electrocatalytic behavior of titania films modified by nitrogen and platinum species. Appl Nanosci 12:565–577. https://doi.org/10.1007/s13204-021-01690-1

Ijadpanah-Saravy H, Safari M, Khodadadi-Darban A, Rezaei A (2014) Synthesis of titanium dioxide nanoparticles for photocatalytic degradation of cyanide in wastewater. Anal Lett 47:1772–1782. https://doi.org/10.1080/00032719.2014.880170

Inada M, Mizue K, Enomoto N, Hojo J (2009) Synthesis of rutile TiO_2 with high specific surface area by self-hydrolysis of $TiOCl_2$ in the presence of SDS. J Ceram Soc Jpn 117:819–822. https://doi.org/10.2109/jcersj2.117.819

Islam SZ, Rankin SE (2016) Hydrazine-based synergistic Ti(III)/N doping of surfactant-templated TiO_2 thin films for enhanced visible light photocatalysis. Mater Chem Phys 182:382–393. https://doi.org/10.1016/j.matchemphys.2016.07.046

Islam SZ, Reed A, Kim DY, Rankin SE (2016) N_2/Ar plasma induced doping of ordered mesoporous TiO_2 thin films for visible light active photocatalysis. Microporous Mesoporous Mater 220:120–128. https://doi.org/10.1016/j.micromeso.2015.08.030

Jaafar NF, Jalil AA, Triwahyono S, Muhid MNM, Sapawe N, Satar MAH, Asaari H (2012) Photodecolorization of methyl orange over α-Fe_2O_3-supported HY catalysts: the effects of catalyst preparation and dealumination. Chem Eng J 191:112–122. https://doi.org/10.1016/j.cej.2012.02.077

Jaafar NF, Jalil AA, Triwahyono S, Efendi J, Mukti RR, Jusoh R, Jusoh NWC, Karim AH, Salleh NFM, Suendo V (2015a) Direct in situ activation of Ag^0 nanoparticles in synthesis of Ag/TiO_2 and its photoactivity. Appl Surf Sci 338:75–84. https://doi.org/10.1016/j.apsusc.2015.02.106

Jaafar NF, Jalil AA, Triwahyono S, Shamsuddin N (2015b) New insights into self-modification of mesoporous titania nanoparticles for enhanced photoactivity: effect of microwave power density on formation of oxygen vacancies and Ti^{3+} defects. RSC Adv 5:90991–91000. https://doi.org/10.1039/C5RA15120A

Jaafar NF, Jalil AA, Triwahyono S (2017) Visible-light photoactivity of plasmonic silver supported on mesoporous TiO_2 nanoparticles (Ag-MTN) for enhanced degradation of 2-chlorophenol: Limitation of Ag-Ti interaction. Appl Surf Sci 392:1068–1077. https://doi.org/10.1016/j.apsusc.2016.09.112

Jaafar NF, Ahmad ZA, Jusoh NWC, Nagao Y (2019a) X-ray diffraction and spectroscopic studies of microwave synthesized mesoporous titania nanoparticles for photodegradation of 2-chlorophenol under visible light. AIP Conf Proc 2068:1–6. https://doi.org/10.1063/1.5089380

Jaafar NF, Marfur NA, Jusoh NWC, Nagao Y, Kamarudin NHN, Jusoh R, Iqbal MAM (2019b) Synthesis of mesoporous nanoparticles via microwave-assisted method for photocatalytic degradation of phenol derivatives. Malaysian J Anal Sci 23:462–471. https://doi.org/10.17576/mjas-2019b-2303-10

Jaafar NF, Najman AMM, Marfur A, Jusoh NWC (2020) Strategies for the formation of oxygen vacancies in zinc oxide nanoparticles used for photocatalytic degradation of phenol under visible light irradiation. J Photochem Photobiol A 388:1–10. https://doi.org/10.1016/j.jphotochem.2019.112202

Jalil AA, Satar MAH, Triwahyono S, Setiabudi HD, Kamarudin NHN, Jaafar NF, Sapawe N, Ahamad R (2013) Tailoring the current density to enhance photo-catalytic activity of CuO/HY for decolorization of malachite green. J Electroanal Chem 701:50–58. https://doi.org/10.1016/j.jelechem.2013.05.003

Jamila GS, Sajjad S, Leghari SAK, Mehboob M, Flox C (2022) Enhanced electron transport by Fe_2O_3 on NCQDs–MgO nanostructure for solar photocatalysis and electrocatalytic water splitting. Appl Nanosci. https://doi.org/10.1007/s13204-022-02424-7

Jawad AH, Mubarak NSA, Ishak MAM, Ismail K, Nawawi WI (2016) Kinetics of photocatalytic decolourization of cationic dye using porous TiO_2 film. J Taibah Univ Sci 10:352–362. https://doi.org/10.1016/j.jtusci.2015.03.007

Jusoh NWC, Jalil AA, Triwahyono S, Setiabudi HD, Sapawe N, Satar MAH, Karim AH, Kamarudin NHN, Jusoh R, Jaafar NF, Salamun N (2013) Sequential desilication-isomorphous substitution route to prepare mesostructured silica nanoparticles loaded with ZnO and their photocatalytic activity. Appl Catal A 468:276–287. https://doi.org/10.1016/j.apcata.2013.09.005

Jusoh R, Jalil AA, Triwahyono S, Idris A, Haron S, Sapawe N, Jaafar NF, Jusoh NWC (2014) Synthesis of reverse micelle α-FeOOH nanoparticles in ionic liquid as anonly electrolyte: inhibition of electron-hole pair recombination for efficient photoactivity. Appl Catal A 469:33–44. https://doi.org/10.1016/j.apcata.2013.09.046

Jusoh R, Jalil AA, Triwahyono S, Kamarudin NHN (2015) Synthesis of dual type Fe species supported mesostructured silica

nanoparticles: synergistical effects in photocatalytic activity. RSC Adv 5:9727–9736. https://doi.org/10.1039/C4RA13837F

Kakavandi R, Sava AS, Caneshi A, Chasse T, Casu BM (2013) At the interface between organic radicals and TiO_2 (110) single crystals: electronic structure and para-magnetic character. Chem Commun 49:101103–101105. https://doi.org/10.1039/C3CC45693E

Karim AH, Jalil AA, Triwahyono S, Kamarudin NHN, Ripin A (2014) Influence of multi-walled carbon nanotubes on textural and adsorption characteristics of in situ synthesized mesostructured silica. J Colloid Interface Sci 421:93–102. https://doi.org/10.1016/j.jcis.2014.01.039

Khan MM, Ansari SA, Pradhan D, Ansari MO, Lee J, Cho MH (2014) Band gap engineered TiO_2 nanoparticles for visible light induced photoelectrochemical and photocatalytic studies. J Mater Chem A 2:637–644. https://doi.org/10.1039/c3ta14052k

Khanmohammadi M, Shahrouzi JR, Rahmani F (2021) Insights into mesoporous MCM-41-supported titania decorated with CuO nanoparticles for enhanced photodegradation of tetracycline antibiotic. Environ Sci Pollut Res 28:862–879. https://doi.org/10.1007/s11356-020-10546-0

Kim A, Sanchez C, Haye B, Boissiere C, Sassoye C, Debecker DP (2019) Mesoporous TiO_2 support materials for Ru-based CO_2 methanation catalysts. ACS Appl Nano Mater 2019:1. https://doi.org/10.1021/acsanm.9b00518

Kumar D, Moharana A, Kumar A (2020) Current trends in spinel based modified polymer composite materials for electromagnetic shielding. Mater Today Chem 17:100346. https://doi.org/10.1016/j.mtchem.2020.100346

Li KCJ, Wang W, Zhang Y, Wang X, Su H (2012) Effects of surfactants on microstructure and photocatalytic activity of TiO_2 nanoparticles prepared by the hydrothermal method. Mater Sci Semicond Process 15:20–26. https://doi.org/10.1016/j.mssp.2011.05.007

Li W, Liang R, Hu A, Huang Z, Zhou YN (2014a) Generation of oxygen vacancies in visible light activated one-dimensional iodine TiO_2 photocatalysts. RSC Adv 4:36959–36966. https://doi.org/10.1039/C4RA04768K

Li W, Wu Z, Wang J, Elzatahry AA, Zhao D (2014b) A perspective on mesoporous TiO_2 materials. J Chem Mater 26:287–298. https://doi.org/10.1021/cm4014859

Li X, Liu P, Mao Y, Xing M, Zhang J (2015) Preparation of homogeneous nitrogen-doped mesoporous TiO_2 spheres with enhanced visible-light photocatalysis. App Catal B: Environ 164:352–359. https://doi.org/10.1016/j.apcatb.2014.09.053

Mahoney L, Koodali RT (2014) Versatility of Evaporation-Induced Self-Assembly (EISA) method for preparation of mesoporous TiO_2 for energy and environmental applications. Mater 7:2697–2746. https://doi.org/10.3390/ma7042697

Majumder S, Choudhary RJ, Tripathi M, Phase DM (2018) Effect of calcination routes on phase formation of $BaTiO_3$ and their electronic and magnetic properties. AIP Conf Proc 1953:1–4. https://doi.org/10.1063/1.5033045

Marco-Brown JL, Blesa MA, Soler-Illia GJAA (2017) Preparation of mesoporous titania xerogels under controlled synthesis conditions. Effects of processing in the textural, adsorption and photocatalytic properties. Colloids Surf a: Physicochem Eng Aspects 530:93–103. https://doi.org/10.1016/j.colsurfa.2017.07.054

Marfur NA, Jaafar NF (2021a) Mesoporous titania nanoparticles as photocatalyst for degradation of 2-chlorophenol. J Chem Eng Ind Biotechnol 7:32–36. https://doi.org/10.15282/jceib.v7i1.6135

Marfur NA, Jaafar NF (2021b) Insight into the influence of defect sites in mixed phase of mesoporous titania nanoparticles toward photocatalytic degradation of 2-chlorophenol: Effect of light source. J Chin Chem Soc. https://doi.org/10.1002/jccs.202100127

Marfur NA, Jaafar NF, Habibullah NHHM (2019) Electrogenerated iron supported on mesoporous titania nanoparticles for the photocatalytic degradation of 2-chlorophenol. CR Chim 22:813–821. https://doi.org/10.1016/j.crci.2019.08.006

Marfur NA, Jaafar NF, Gani FHH (2020a) Effect of microwave power intensity on synthesis of mesoporous titania nanoparticles for degradation of 2,4-dichlorophenol: Photoactivity performance and kinetic studies. IOP Conf Ser: Mater Sci Eng 736:1–12. https://doi.org/10.1088/1757-899X/736/3/032016

Marfur NA, Jaafar NF, Habibullah NHHM (2020b) Effect of iron loading onto mesoporous titania nanoparticles and its photoactivity. IOP Conf Ser Mater Sci Eng 736:1–9. https://doi.org/10.1088/1757-899X/736/4/042034

Marfur NA, Jaafar NF, Khairuddean M, Nordin N (2020c) A review on recent progression of modifications on titania morphology and its photocatalytic performance. Acta Chim Slov 67:361–374. https://doi.org/10.17344/acsi.2018.5161

Mazinani B, Masrom AK, Beitollahi A, Luque R (2014) Photocatalytic activity, surface area and phase modification of mesoporous SiO_2-TiO_2 prepared by a one-step hydrothermal procedure. Ceram Int 40:11525–11532. https://doi.org/10.1016/j.ceramint.2014.03.071

Meksi M, Berhault G, Guillard C, Kochkar H (2015) Design of TiO_2 nanorods and nanotubes doped with lanthanum and comparative kinetic study in the photodegradation of formic acid. Catal Commun 61:107–111. https://doi.org/10.1016/j.catcom.2014.12.020

Merin KT, Athira K, Raguram T, Rajni KS (2020) Effect of zinc concentration in TiO_2 nanoparticles synthesized by sol-gel technique for photocatalytic applications. Mater Today: Proc. https://doi.org/10.1016/j.matpr.2020.04.516

Miao Z, Wang G, Zhang X, Dong X (2020) Oxygen vacancies modified TiO_2/Ti_3C_2 derived from MXenes for enhanced photocatalytic degradation of organic pollutants: the crucial role of oxygen vacancy to schottky junction. Appl Surf Sci 528:146929. https://doi.org/10.1016/j.apsusc.2020.146929

Mohamed RM, Zak ZI (2020) Degradation of Imazapyr herbicide using visible light-active CdO-TiO_2 heterojunction photocatalyst. J Environ Chem Eng. https://doi.org/10.1016/j.jece.2020.104732

Moharana A, Kumar A, Thakur A, Vo DVN, Sharma A, Kumar D (2021) Chapter 6—role of nanostructured metal oxides in photocatalysis: An overview. Nanostruct Photocatalysts. https://doi.org/10.1016/B978-0-12-823007-7.00010-9

Munoz M, de Pedro ZM, Casas JA, Rodriguez JJ (2011) Assessment of the generation of chlorinated byproducts upon Fenton-like oxidation of chlorophenols at different conditions. J Hazard Mater 190:993–1000. https://doi.org/10.1016/j.jhazmat.2011.04.038

Nagpure S, Zhang Q, Khan MA, Islam SZ, Xu J, Strzalka J, Cheng YT, Knutson BL, Rankin SE (2018) Layer-by-layer synthesis of thick mesoporous TiO_2 films with vertically oriented accessible nanopores and their application for lithium-ion battery negative electrodes. Adv Funct Mater 2018:1–10. https://doi.org/10.1002/adfm.201801849

Navarrete BT, Delgado FP, Sicairos SP (2020) Structure, microstructure and surface of Nd^{3+}-doped mesoporous anatase-phase TiO_2. Appl Phys A 126:592–599. https://doi.org/10.1007/s00339-020-03768-z

Noman MT, Ashraf MA, Ali A (2019) Synthesis and applications of nano-TiO_2: a review. Environ Sci Pollut Res 26:3262–3291. https://doi.org/10.1007/s11356-018-3884-z

Nur AS, Sultana M, Mondal A, Islam S, Robel FN, Islam MA, Sumi MSA (2022) A review on the development of elemental and codoped TiO_2 photocatalysts for enhanced dye degradation under UV–vis irradiation. J Water Process Eng 47:102728. https://doi.org/10.1016/j.jwpe.2022.102728

Padmanabhan NT, Jayaraj MK, John H (2018) Mechanistic insights into CTAB assisted TiO_2 crystal growth with largely exposed high energy crystal facets. J Environ Chem Eng 6:5510–5519. https://doi.org/10.1016/j.jece.2018.08.045

Pal M, Wan L, Zhu Y, Liu Y, Liu Y, Gao W, Li Y, Zheng G, Elzatahry AA, Alghamdi A, Deng Y, Zhao D (2016) Scalable synthesis of mesoporous titania microspheres via spray-drying method. J Colloid Interface Sci 479:150–159. https://doi.org/10.1016/j.jcis.2016.06.063

Pan X, Yang MQ, Fu X, Zhang N, Xu YJ (2013) Defective TiO_2 with oxygen vacancies: synthesis, properties and photocatalytic applications. Nanoscale 5:3601–3614. https://doi.org/10.1039/c3nr00476g

Pascual AMD, Valles C, Mateos R, Lopez SV, Kinloch IA, Andres MPS (2018) Influence of surfactants of different nature and chain length on the morphology, thermal stability and sheet resistance of graphene. Soft Matter 14:6013–6023. https://doi.org/10.1039/C8SM01017J

Pathak SS, Pius IC, Bhanushali RD, Pillai KT, Dehadraya JV, Mukerjee SK (2013) Effect of surfactants on the morphology of titania microspheres prepared by internal gelation process. J Porous Mater 20:753–761. https://doi.org/10.1007/s10934-012-9650-6

Pato AH, Balouch A, Talpur FN, Abdullah PP, Mahar AM, Jagirani MS, Kumar S, Sanam S (2021) Fabrication of TiO_2@ITO-grown nanocatalyst as efficient applicant for catalytic reduction of Eosin Y from aqueous media. Environ Sci Pollut Res 28:947–959. https://doi.org/10.1007/s11356-020-10548-y

Payormhorm J, Chuangchote S, Laosiripojana N (2017) CTAB-assisted sol-microwave method for fast synthesis of mesoporous TiO_2 photocatalysts for photocatalytic conversion of glucose to value-added sugars. Mater Res Bull 95:546–555. https://doi.org/10.1016/j.materresbull.2017.08.016

Pijarn N, Jeimsirilers S, Jinawath S (2013) Photocatalytic activity of mixed phase TiO_2 from microwave-assisted synthesis. Adv Mater Res 664:661–666. https://doi.org/10.4028/www.scientific.net/AMR.664.661

Prathyusha KR, Sreenivasan KP (2020) Synthesis of Na^+/$Ca2^+$ ions modified TiO_2 xerogels through co precipitation method. Indian J Chem 59:747–751

Rad AS, Afshar A, Azadeh M (2020) Anti-reflection and self-cleaning meso-porous TiO_2 coatings as solar systems protective layer: investigation of effect of porosity and roughness. Opt Mater 107:1–9. https://doi.org/10.1016/j.optmat.2020.110027

Rafiee E, Noori E, Zinatizadeh AA, Zangeneh H (2018) Surfactant effect on photocatalytic activity of Ag-TiO_2/PW nanocomposite in DR16 degradation: characterization of nanocomposite and RSM process optimization. Mater Sci Semicond Process 83:115–124. https://doi.org/10.1016/j.mssp.2018.04.021

Rahman NRA, Muniandy L, Adam F, Iqbal A, Ng EP, Lee HL (2019) Detailed photocatalytic study of alkaline titanates and its application for the degradation of methylene blue (MB) under solar irradiation. J Photochem Photobiol A 375:219–230. https://doi.org/10.1016/j.jphotochem.2019.02.020

Ramimoghadam D, Hussein MZ, Taufiq-Yap YH (2012) The effect of sodium dodecyl sulfate (SDS) and cetyltrimethylammonium bromide (CTAB) on the properties of ZnO synthesized by hydrothermal method. Int J Mol Sci 13:13275–13293. https://doi.org/10.3390/ijms131013275

Rashid J, Barakat MA, Pettit SL, Kuhn JN (2014) $InVO_4$/TiO_2 composite for visible-light photocatalytic degradation of 2-chlorophenol in wastewater. Environ Tech 35:2153–2159

Ravishankar TN, de O Vaz M, Teixeira SR, (2020) The effect of surfactant on sol-gel synthesis of CuO/TiO_2 nanocomposites for the photocatalytic activities under UV-visible and visible light illuminations. New J Chem 44:1888–1904. https://doi.org/10.1039/C9NJ05246A

Reinosa JJ, Docio CMA, Ramirez VZ, Lozano JFF (2018) Hierarchical nano ZnO-micro TiO_2 composites: High UV protection yield lowering photodegradation in sunscreens. Ceram Int 44:2827–2834. https://doi.org/10.1016/j.ceramint.2017.11.028

Ren R, Wen Z, Cui S, Hou Y, Guo X, Chen J (2015) Controllable synthesis and tunable photocatalytic properties of Ti^{3+}-doped TiO_2. Sci Rep 5:1–11. https://doi.org/10.1038/srep10714

Ruzicka JY, Bakar FA, Thomsen L, Cowie BC, Nicoll CM, Kemmitt T, Brand HEA, Ingham B, Andersson GG, Golovko VB (2014) XPS and NEXAFS study of fluorine modified TiO_2 nano-ovoids reveals dependence of Ti^{3+} surface population on the modifying agent. RSC Adv 4:20649–20658. https://doi.org/10.1039/c3ra47652a

Saavedra LCC, Gomez EMP, Oliveira RG, Fernandez MA (2017) Aggregation behaviour and solubilization capability of mixed micellar systems formed by a gemini lipoamino acid and a non-ionic surfactant. Colloids Surf A 533:41–47. https://doi.org/10.1016/j.colsurfa.2017.08.011

Salleh MAM, Mahmoud DK, Karim WAWA, Idris A (2011) Cationic and anionic dye adsorption by agricultural solid wastes: a comprehensive review. Desalin 280:1–13. https://doi.org/10.1016/j.desal.2011.07.019

Samsudin EM, Hamid SBA, Juan JC, Basirun WJ (2015) Influence of triblock copolymer (pluronic F127) on enhancing the physicochemical properties and photocatalytic response of mesoporous TiO_2. App Surf Sci 355:959–968. https://doi.org/10.1016/j.apsusc.2015.07.178

Sapawe N, Jalil AA, Triwahyono S, Adam SH, Jaafar NF, Satar MAH (2012) Isomorphous substitution of Zr in the framework of aluminosilicate HY by an electrochemical method: Evaluation by methylene blue decolorization. Appl Catal B: Environ 125:311–323. https://doi.org/10.1016/j.apcatb.2012.05.042

Sapawe N, Jalil AA, Triwahyono S (2013a) One-pot electro-synthesis of ZrO_2-ZnO/HY nanocomposite for photocatalytic decolorization of various dye-contaminants. Chem Eng J 225:254–265. https://doi.org/10.1016/j.cej.2013.03.121

Sapawe N, Jalil AA, Triwahyono S, Sah RNRA, Jusoh NWC, Hairom NHH, Efendi J (2013b) Electrochemical strategy for grown ZnO nanoparticles deposited onto HY zeolite with enhanced photodecolorization of methylene blue: effect of the formation of Si O Zn bonds. Appl Catal A 456:144–158. https://doi.org/10.1016/j.apcata.2013.02.025

Saravanan R, Karthikeyan S, Gupta VK, Sekaran G, Narayanan V, Stephen A (2013a) Enhanced photocatalytic activity of ZnO/CuO nanocomposite for the degradation of textile dye on visible light illumination. Mater Sci Eng C. https://doi.org/10.1016/j.msec.2012.08.011

Saravanan R, Thirumal E, Gupta VK, Narayanan V, Stephen A (2013b) The photocatalytic activity of ZnO prepared by simple thermal decomposition method at various temperatures. J Mol Liq 177:394–401. https://doi.org/10.1016/j.molliq.2012.10.018

Savaliya C, Kundaliya H, Jethva S, Katba S, Ravalia A, Kuberkar DG (2022) Role of Ba and Ti co-doping in modifying the structural, electrical and magnetic properties of $LaFeO_3$ films. Appl Nanosci. https://doi.org/10.1007/s13204-021-02192-w

Shah I, Adnan R, Wan Ngah WS, Mohamed N (2015) Iron impregnated activated carbon as an efficient adsorbent for the removal of methylene blue: regeneration and kinetics studies. PLoS ONE 10:1–23. https://doi.org/10.1371/journal.pone.0122603

Sharma A, Lee BK (2016) Rapid photo-degradation of 2-chlorophenol under visible light irradiation using cobalt oxide-loaded TiO_2/reduced graphene oxide nanocomposite from aqueous media. J Environ Manage 165:1–10

Shayesteh H, Raji F, Kelishami AR (2021) Influence of the alkyl chain length of surfactant on adsorption process: a case study. Surf Interfaces 22:1–10. https://doi.org/10.1016/j.surfin.2020.100806

Sheikhnejad-Bishe O, Zhao F, Rajabtabar-Darvishi A, Khodadad E, Mostofizadeh A, Huang Y (2014) Influence of temperature and surfactant on the photocatalytic performance of TiO_2 nanoparticles. Int J Electrochem Sci 9:4230–4240

Shouman MA, Fathy NA (2018) Microporous nanohybrids of carbon xerogels and multi-walled carbon nanotubes for removal of rhodamine B dye. J Water Process Eng 23:165–173. https://doi.org/10.1016/j.jwpe.2018.03.014

Simon SM, George G, Chandran A, Prakashan VP, Sajna MS, Saritha AC, Biju PR, Joseph C, Unnikrishnan NV (2020) Morphological and thermal studies of mesoporous TiO_2-ZrO_2 and TiO_2-ZrO_2-polymer composites as potential self-cleaning surface. Mater Today: Proc 33:1327–1332. https://doi.org/10.1016/j.matpr.2020.04.181

Singh J, Kumar D, Kumar PS, Huerta Aguilar CA, Vo D-VN, Sharma A, Kaur H (2021) Magnetically active Ag–Zn nanoferrites synthesized by solution combustion route: physical chemical studies and density functional theory analysis. Mater Today Chem 22:100588. https://doi.org/10.1016/j.mtchem.2021.100588

Smirnova N, Petrik I, Vorobets V, Kolbasov G, Eremenko A (2017) Sol-gel synthesis, photo- and electrocatalytic properties of mesoporous TiO_2 modified with transition metal ions. Nanoscale Res Lett 12:239. https://doi.org/10.1186/s11671-017-2002-3

Song S, Wang C, Hong F, He Z, Cai Q, Chen J (2011) Gallium- and iodine-co-doped titanium dioxide for photocatalytic degradation of 2-chlorophenol in aqueous solution: Role of gallium. App Surf Sci 257:3427–3432

Su C, Shao C, Liu Y (2011) Electrospun nanofibers of TiO_2/CdS heteroarchitectures with enhanced photocatalytic activity by visible light. J Colloid Interface Sci 359:220–227. https://doi.org/10.1016/j.jcis.2011.03.044

Sun B, Zhou G, Shao C, Jiang B, Pang J, Zhang Y (2014) Spherical mesoporous TiO_2 fabricated by sodium dodecyl sulfate-assisted hydrothermal treatment and its photocatalytic decomposition of papermaking wastewater. Powder Technol 256:118–125. https://doi.org/10.1016/j.powtec.2014.01.094

Szekely I, Baia M, Magyari K, Boga B, Pap Z (2019) The effect of the pH adjustment upon the WO_3-WO_3·0.33H_2O-TiO_2 ternary composite systems' photocatalytic activity. Appl Surf Sci 490:469–480. https://doi.org/10.1016/j.apsusc.2019.06.036

Tzikalos N, Belessi V, Lambropoulou D (2012) Photocatalytic degradation of Reactive Red 195 using anatase/brookite TiO_2 mesoporous nanoparticles: optimization using response surface methodology (RSM) and kinetics studies. Environ Sci Pollut Res 20:2305–2320. https://doi.org/10.1007/s11356-012-1106-7

Vasilopoulou M (2014) Effect of surface hydrogenation of metal oxides on the nano-morphology and the charge generation efficiency of polymer blend solar cells. Nanoscale 6:13726–13739. https://doi.org/10.1039/C4NR04408H

Wahyuningsih S, Ramelan AH, Juliana G, Khoirunisa AR, Rahardjo SB, Pramono E, Suharyana S, Suryana R, Supriyanto A (2014) Synthesis of high surface area titanium dioxide by sol gel process for DSSC. Proc SPIE 9137:1–13. https://doi.org/10.1117/12.2052263

Wang X, Li Y, Liu X, Gao S, Huang B, Dai Y (2015a) Preparation of Ti^{3+} self-doped TiO_2 nanoparticles and their visible light photocatalytic activity. Chin J Catal 36:389–399. https://doi.org/10.1016/S1872-2067(14)60234-5

Wang Y, Sun H, Ang HM, Tade MO, Wang S (2015b) 3D-hierarchically structured MnO_2 for catalytic oxidation of phenol solutions by activation of peroxymonosulfate: Structure dependence and mechanism. Appl Catal B: Environ 164:159–167. https://doi.org/10.1016/j.apcatb.2014.09.004

Wang Y, Pan F, Dong W, Xu L, Wu K, Xu G, Chen W (2016) Recyclable silver-decorated magnetic titania nanocomposite with enhanced visible-light photocatalytic activity. Appl Catal B: Environ 189:192–198. https://doi.org/10.1016/j.apcatb.2016.02.057

Wang X, Zhang L, Bu Y, Sun W (2021) Interplay between invasive single atom Pt and native oxygen vacancy in anatase TiO_2 (1 0 1) surface: a theoretical study. Appl Surf Sci 540:1–9. https://doi.org/10.1016/j.apsusc.2020.148357

Wei S, Wang F, Dan M, Zeng K, Zhou Y (2017) The role of high oxygen vacancy concentration on modification of surface properties and H_2S adsorption on the rutile TiO_2 (110). Appl Surf Sci 422:990–996. https://doi.org/10.1016/j.apsusc.2017.06.040

Wei J, Wen X, Zhu F (2018) Influence of surfactant on the morphology and photocatalytic activity of anatase TiO_2 by solvothermal synthesis. J Nanomater 2018:1–7. https://doi.org/10.1155/2018/3086269

Wei Y, Li Y, Han D, Liu J, Lyu S, Li C, Tan Y, Wang Z, Yu J (2022) Facile strategy to construct porous CuO/CeO_2 nanospheres with enhanced catalytic activity toward CO catalytic oxidation at low temperature. Appl Nanosci. https://doi.org/10.1007/s13204-021-02334-0

Wu W, Zhang L, Zhai X, Liang C, Yu K (2018) Preparation and photocatalytic activity analysis of nanometer TiO_2 modified by surfactant. Nanomater Nanotechnol 8:1–8. https://doi.org/10.1177/1847980418781973

Xu G, Zhang Y, Peng D, Sheng D, Tian Y, Ma D, Zhang Y (2021) Nitrogen-doped mixed-phase TiO_2 with controllable phase junction as superior visible-light photocatalyst for selective oxidation of cyclohexane. Appl Surf Sci 536:147953. https://doi.org/10.1016/j.apsusc.2020.147953

Yagub MT, Sen TK, Afroze S, Ang HM (2014) Dye and its removal from aqueous solution by adsorption: A review. Adv Colloid Interface Sci 209:172–184. https://doi.org/10.1016/j.cis.2014.04.002

Yuan C, Hung CH, Li HW, Chang WH (2016) Photodegradation of ibuprofen by TiO_2 co-doping with urea and functionalized CNT irradiated with visible light-Effect of doping content and pH. Chemosphere 155:471–478. https://doi.org/10.1016/j.chemosphere.2016.04.055

Yuenyongsuwana J, Nithiyakorna N, Sabkirda P, O'Rearc EA, Pongprayoon T (2018) Surfactant effect on phase-controlled synthesis and photocatalyst property of TiO_2 nanoparticles. Mater Chem Phys 214:330–336. https://doi.org/10.1016/j.matchemphys.2018.04.111

Zhou WJ, Fang L, Fan Z, Albela B, Bonneviot L, Campo FD, Pera-Titus M, Clacens J (2014) Tunable catalysts for solvent-free biphasic systems: pickering interfacial catalysts over amphiphilic silica nanoparticles. J Am Chem Soc 136:4869–4872. https://doi.org/10.1021/ja501019n

Zhou Q, Li L, Wang J, Zhang X, Zhou S (2019) Synergistic effect of ZnO QDs and Sn^{4+} ions to control anatase-rutile phase of three-dimensional ordered hollow sphere TiO_2 with enhanced photodegradation and hydrogen evolution. Appl Surf Sci 481:1185–1195. https://doi.org/10.1016/j.apsusc.2019.03.170